Effect of Target Properties and Impact Velocity on Ejection Dynamics and Ejecta Deposition

Robert Luther[1], Meng-Hua Zhu[1,2], Gareth Collins[3], Kai Wünnemann[1,4]

[1]Museum für Naturkunde Berlin, Leibniz Institute for Evolution and Biodiversity Science, Berlin, Germany

[2]Space Science Institute, Macau University of Science and Technology, Taipa, Macau

[3]Department of Earth Science & Engineering, Imperial College London, London, UK

[4]Institute of Geological Sciences, Freie Universität Berlin, Germany

Abstract

Impact craters are formed by the displacement and ejection of target material. Ejection angles and speeds during the excavation process depend on specific target properties. In order to quantify the influence of the constitutive properties of the target and impact velocity on ejection trajectories we present the results of a systematic numerical parameter study. We have carried out a suite of numerical simulations of impact scenarios with different coefficients of friction (0.0 – 1.0), porosities (0% - 42%) and cohesions (0 MPa – 150 MPa). Furthermore, simulations with varying pairs of impact velocity (1-20 km/s) and projectile mass yielding craters of approximately equal volume are examined. We record ejection speed, ejection angle, and the mass of ejected material to determine parameters in scaling relationships, and to calculate the thickness of deposited ejecta by assuming analytical parabolic trajectories under Earth gravity. For the resulting deposits we parameterise the thickness as a function of radial distance by a power law. We find that strength—that is, the coefficient of friction and target cohesion—has the strongest effect on the distribution of ejecta. In contrast, ejecta thickness as a function of distance is very similar for different target porosities and for varying impact velocities larger than ~6 km/s. We compare the derived ejecta deposits with observations from natural craters and experiments.

Introduction

Crater formation is one of the most ubiquitous processes in our solar system. Most planetary surfaces are dominated by impact craters and their surrounding ejecta blankets. As long ago as the end of the 18th century, the astronomer Johann Hieronymus Schröter observed

crater rims ("Ringgebirge") and crater cavities ("Wallebene") on the Moon and, after comparing their masses, proposed a common explosive process that may have caused the excavation of material (Schröter 1791).

During the cratering process, energy and momentum are transferred from the projectile onto the target, causing material movement (e.g. Wegener 1921; Schmidt 1980). Parts of the material are displaced into the expanding cavity, while other parts are ejected out of the cavity on ballistic trajectories. Most of the debris ejected from a crater is deposited within two crater radii as a more-or-less continuous ejecta blanket whose characteristics depend on the distance from the point of impact, target properties, and the presence or absence of an atmosphere.

The study of ejected material is important for the understanding of the evolution of the solar system: impact cratering and the formation of ejecta deposits are a dominant resurfacing process on most objects in the solar system. Near-rim ejecta deposits are a morphological unit where impactites and shock metamorphosed rocks can be found (e.g. Stöffler et al., (1975), and reveal valuable information for studying crater formation mechanics. Fast ejecta can escape the gravitational field of its parent body and can collide with other bodies, transporting material to them (Head et al. 2002; Artemieva and Ivanov 2004; Alvarellos et al. 2008). Thus, ejection dynamics have consequences for early planetary accretion, and collisional evolution of asteroids (e.g. Farinella and Davis 1992; Campo Bagatin et al. 1994). In contrast, ejected material that does not escape the gravity field of its parent body can cause a series of secondary impacts producing a regolith layer on the surface by fracturing of local material and mixture with the ejected material (e.g. Oberbeck 1975).

The study of ejecta dynamics has been conducted in laboratory experiments for different target and projectile materials, and for different impact velocities. In some of the earliest work ejection speed was measured indirectly, by tagging target material prior to impact (or explosion) and locating its post-impact/explosion position (Stöffler et al. 1975; Piekutowski 1980). By necessity, this procedure assumes a constant ejection angle and that ejected material follows a simple ballistic parabola from the launch position to the landing site, with no subsequent outward flow, sliding, or rolling. The experiments by Stöffler et al. (1975) also investigated shock loading of ejecta in order to derive the relative amount of shocked material in the final ejecta distribution. A similar approach was followed by recent impact experiments into competent rock, reconstructing ejecta trajectories from ejecta catchers mounted opposite the target parallel to the surface (Sommer et al. 2013). More recently, both ejection angle and speed were measured directly, in a novel suite of experiments using systems of lasers and cameras to illuminate the ejecta and track its

movement in time (Gulde et al. this issue; Cintala et al. 1999; Anderson and Schultz 2003; Anderson et al. 2004; Anderson and Schultz 2006; Hermalyn and Schultz 2010, 2011; Hermalyn et al. 2012; Tsujido et al. 2015). Some studies are able to track individual particles or give at least a particle size distribution for their total detected ejected material (Gulde et al. this issue; Buhl et al. 2014). These experiments provide empirical relationships between ejection speed and angle and launch position within the crater for a number of different target materials (Housen et al. 1983; Housen and Holsapple 2011); however, as it is difficult to isolate the effect of individual target properties on ejection characteristics in experiments, the dominant controls on ejecta behaviour remain unclear.

Numerical impact simulations permit the investigation of the effect of individual material properties (such as porosity, cohesion and friction coefficient) on the cratering process thereby allowing a very wide variation in material behaviour to be studied. Such simulations also allow the use of impact velocities and impactor sizes that are much larger than is possible in laboratory experiments. Previous numerical studies analysed the ejection behaviour in models for specific impact set-ups (Wada et al. 2006; Hermalyn and Schultz 2011; Zhu et al. 2015; Wünnemann et al. 2016). In this study that was conducted in the framework of the Multidisciplinary Experimental and Modeling Impact Research Network (MEMIN, e.g. Kenkmann et al. this issue), we use numerical modelling to systematically investigate the effect of several important target material properties on the ejection velocity vector (speed and angle) as a function of launch position within the growing crater. The results are used to predict the amount of ejecta landing on the surface as a function of distance assuming ballistic trajectories in the absence of an atmosphere.

THEORETICAL BACKGROUND

Impact cratering has been studied at a variety of scales in both laboratory and numerical experiments. Scaling relationships (e.g., Housen et al. 1983) relating impactor and target parameters, such as projectile radius a, impact velocity v_i or target gravity g on the one hand side, to crater characteristics, such as the transient crater radius R or volume V on the other side, have been developed to allow for direct comparison of laboratory experiments with natural craters. With all impact parameters known, the outcome (crater size and ejecta distribution) of an impact scenario can be approximated with such scaling relationships. In the following, we introduce some of the concepts from literature that we will use later on. Note that we only consider vertical impacts.

In the early stage of an impact, the projectile transfers energy and momentum onto the target. In scaling theory, this transfer is parameterized by a single coupling parameter C (Holsapple 1981):

$$C = a\, v_i^{\mu}\, \delta^{\nu} \quad , \tag{1}$$

where μ is a material dependent parameter with theoretical upper and lower limits of 2/3 (energy scaling) and 1/3 (momentum scaling), respectively, ν is an exponent that is typically set to 1/3, and δ is the projectile density.

At the contact between the projectile and target, a shock wave is generated and propagates through the target (and projectile), causing also an increase in particle velocity within the material as a consequence. Close to the impact point, the material moves approximately in a radial direction from the centre (Figure 1). The shock wave is followed by a rarefaction wave originating from the free surface, which causes an upward pressure gradient and adds an upward component to the velocity field (Gault et al. 1968; Thomsen et al. 1979; Melosh 1989). As a result, during the excavation flow material moves along streamlines that curve upward toward the target surface. Material moving along streamlines that intersect the free surface inside the crater is 'ejected'—is called ejecta—and subsequently follows a ballistic trajectory. The contour of ejected material which intersects the target surface at the edge of the growing cavity, separates ejecta above from material displaced by the subterranean excavation flow (Figure 1). This latter material forms the floor, walls and uplifted rim of the transient crater. The size of the transient crater, i.e. radius R or volume V, can be estimated by scaling relationships and depends on parameters as described by Housen et al. (1983):

$$R = R\left(C, \rho, Y_{eff}, \Phi, g\right) \quad , \tag{2}$$
$$V = V\left(C, \rho, Y_{eff}, \Phi, g\right) \quad ,$$

with the target density ρ, an effective measure of the target strength Y_{eff} and the target porosity Φ. Combining Eq. (1) and (2) in a dimensional analysis yields a non-dimensional equation of the following type as described by e.g. Holsapple (1993). Here, we give a form that is valid in the gravity dominated regime:

$$\pi_V = K_1 \, \pi_2^{-\frac{3\mu}{2+\mu}} \left(\frac{\rho}{\delta}\right)^{-\frac{6\nu-2-\mu}{2+\mu}} \quad , \tag{3}$$

where K_1 is a constant, and Π_V and Π_2 dimensionless parameters:

$$\pi_V = \frac{\rho \, V}{\delta \, V_{pr}} \quad ,$$
$$\pi_2 = 1.61 \, \frac{2a \, g}{v_i^2} \quad , \tag{4}$$

with the projectile volume V_{pr}.

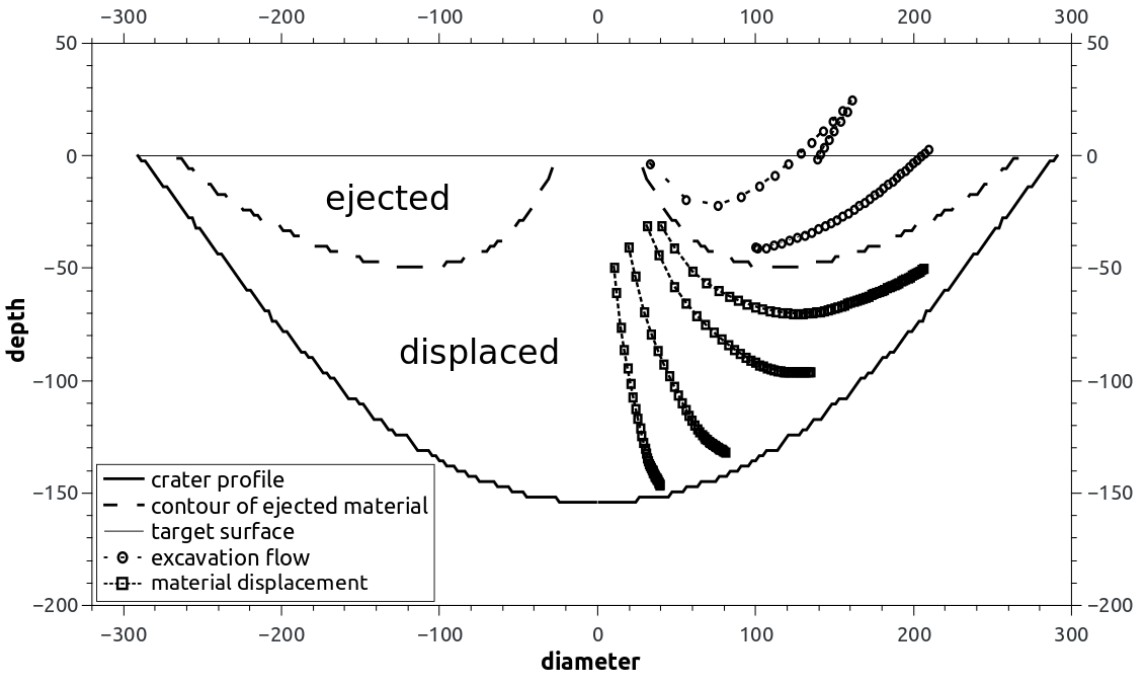

Figure 1: Excavation and material displacement. Trajectories are shown for some exemplary material trajectories within the excavation flow. Material above the dashed line is ejected from the growing cavity, whereas material underneath is displaced within the crater. Note that depending on the target properties material at similar launch positions can experience slightly different ejection angles, as the trajectories indicate. The figure was created from a model described in the results section (coefficient of friction of 0.6, no porosity, no cohesion, impact velocity 6 km/s). The impact site is at the centre.

Assuming a constant gravity field and the absence of an atmosphere or vapour plume, and neglecting any interaction between the ejected particles that might occur due to similar direction of movement of particles, the ejected material will follow parabolic trajectories that

146 are defined by an initial ejection speed and ejection angle at a certain launch position. Note
147 that we use both term “ejection” and “launch” interchangeably. These characteristics are
148 closely connected with the material flow within the target prior to ejection and as such are
149 subject to specific material properties that we focus on in this study. Ejection velocities v_{ej}
150 relate to other parameters as follows:
151

$$v_{ej} = v_{ej}\left(C, \rho, Y_{eff}, \Phi, g, x\right) \quad , \tag{5}$$

152
153 with the launch position x. At sufficient distance inward from the crater rim (x/R<1), the
154 kinetic energy of the ejecta is large compared to what is needed to lift it above the surface
155 and, thus, strength and gravity can be neglected (Housen et al. 1983). Using this
156 simplification, and by combining Eq. (1) and (5) with dimensional analysis, it can be assumed
157 that:
158

$$x\, v_{ej}^{\mu}\, \rho^{\nu} \;\sim\; C = a\, v_i^{\mu}\, \delta^{\nu} \quad . \tag{6}$$

159
160 Eq. (6) accounts for the density contrast between target and impactor. Rewriting of this
161 relationship as equation gives (Housen and Holsapple 2011):
162

$$\frac{v_{ej}}{v_i} = K_2 \left(\frac{x}{a}\left(\frac{\rho}{\delta}\right)^{\upsilon}\right)^{-\frac{1}{\mu}} \quad , \tag{7}$$

163
164 where K_2 is a fitting constant. This relationship holds true for most of the range of launch
165 positions (approximately 1.2 a ≤ x < R, Housen and Holsapple 2011). However, close to the
166 impact point, the assumption of a point source and the single coupling parameter C does not
167 hold true. On the other hand, at positions close to the crater rim, ejection velocities are
168 overestimated by this scaling relationship and are better described by adding a factor to the
169 equation above (Housen and Holsapple 2011):
170

$$\frac{v_{ej}}{v_i} = K_2 \left(\frac{x}{a}\left(\frac{\rho}{\delta}\right)^{\upsilon}\right)^{-\frac{1}{\mu}} \left(1 - \frac{x}{a}\,\frac{a}{n\,R}\right)^{p} \quad , \tag{8}$$

171
172 with the transient crater radius R and the fitting parameters p and n. Note, that a/R in the last
173 position gives an inverse measure of cratering efficiency; Eq. (4) states: $\pi_V \sim (R/a)^3$.

The previous expressions used impactor parameters to normalise the physical parameters. This approach is useful to predict the cratering results from known impact parameters. However, the inverse is sometimes required. Instead of using impactor parameters, ejection velocities can also be expressed relative to transient crater radius and gravity by combining Eqs. (2) and (5) in a non-dimensional expression:

$$x\, v_{ej}^{\mu} \;\sim\; R\,\sqrt{gR}^{\,\mu} \quad . \tag{9}$$

Rewriting of this relation as equation gives (Housen et al. 1983):

$$\frac{v_{ej}}{\sqrt{gR}} = K_3 \left(\frac{x}{R}\right)^{-\frac{1}{\mu}} \quad , \tag{10}$$

with the constant K_3 that relates to K_2 as:

$$K_3 = K_2 \frac{v_i}{\sqrt{gR}} \left(\frac{R}{a}\right)^{-\frac{1}{\mu}} \quad . \tag{11}$$

Based on scaling relationships, a theoretical expression for the thickness T of the deposited ejecta as a function of landing distance can be derived. Following the old idea of relating the cavity volume with the volume of material around the crater (Schröter 1791), the volume of ejected material can be related to the integral over the thickness of the blanket (i.e. volume of blanket material) as was done by Housen et al. (1983). Note that only a fraction of the cavity volume is ejected. Using the relationship of ballistic trajectories for flat surfaces and an approximation for a far-field solution, Housen et al. (1983) obtain the following relationship for the thickness of the deposited ejecta over distance in the gravity regime:

$$\frac{T}{R} = K_4 \frac{3\mu}{4\pi} (\sin 2\vartheta)^{\frac{3\mu}{2}} \left(\frac{x}{R}\right)^{-\frac{3\mu+4}{2}} \quad , \tag{12}$$

with the constant K_4 and the launch angle (relative to the horizontal). This simple power-law approximation assumes that all ejecta emanates from the centre of the crater and, thus, is strictly valid only beyond some distance from the crater (approximately 2-3 crater radii,

depending on crater size). A simple power-law expression based on observations was formulated by McGetchin et al. (1973) and modified by Pike (1974):

$$T(r) = T_0 \left(\frac{x}{R}\right)^{-B} \quad , \tag{13}$$

where T_0 is the thickness at the crater rim ($T_0 \sim R$) and B is an exponent. Comparing both Eqs. (12) and (13) gives a correlation between the exponent B and the scaling parameter μ:

$$B = \frac{3\mu + 4}{2} \quad <=> \quad \mu = \frac{2\,B - 4}{3} \quad . \tag{14}$$

However, we again note that a simple power-law ejecta thickness distribution is not expected close to the crater rim.

The set of consistent equation Eqs. (1) - (12) relates different observables like ejection velocity or crater size with projectile parameters such as a and v_i or crater parameters such as R and $\sqrt{gR}$. They are based on a number of idealised assumptions, the most fundamental of which is the assumption of a single coupling parameter as shown in Eq. (1) that combines the three projectile parameters a, v_i and δ (Housen et al. 1983). From the set of scaling relationships, the scaling coefficient μ can be derived from various measurements (e.g., crater size, Eq. (1); ejection velocity, Eqs. (7), (8) & (10); or ejecta deposits, Eq. (12)). However, previous studies (Cintala et al. 1999; Yamamoto et al. 2017) have shown that the determined value of μ from different observational approaches may not be consistent, hinting at a limitation of the idealised concept of scaling relationships.

Scaling relationships suggest that the impact process at different scales and different gravities are directly comparable. However, care is required when applying these equations to large-scale craters on planetary surfaces. The crater diameter (or volume) scaling equations are underpinned by measurements of the final crater diameter in small-scale laboratory experiments, often measured at the preimpact surface, whereas the diameters of natural craters are typically measured at the topographic rim. More significantly, crater enlargement by collapse of the crater rim becomes increasingly important with increasing crater size. At the laboratory scale the difference between final (post-collapse) and transient (pre-collapse) crater radius (at the preimpact level) is typically <10% (e.g. Ormö et al. 2015; Wünnemann et al. 2016). For natural simple craters the difference is estimated to be ~20% (e.g. Melosh 1989). For complex craters different relationships to estimate the ratio between final crater radius R_{final} and transient crater radius R have been suggested by different authors (e.g. Croft 1985;

231 Holsapple 1993; Krüger et al. 2017). They all assume that the gravity driven enlargement of
232 the transient crater results in a much larger ratio between final crater and transient crater
233 radius in the case of complex crater formation. In the present study we do not model any
234 crater modification processes; our simulations are stopped at the end of the excavation stage
235 and crater dimensions used in the ejecta scaling relationships refer to those of the transient
236 crater. For explicit comparison with experimental results where the final rim-to-rim diameter
237 has been measured we estimate the apparent crater diameter by assuming a 10% reduction in
238 diameter from the rim-to-rim diameter.
239

240 # METHODS

241 In this study, we use the iSALE-2D Eulerian shock physics code (Wünnemann et al.
242 2006), which is based on the SALE hydrocode solution algorithm (Amsden et al. 1980). To
243 simulate impact processes in solid materials, SALE was modified to include an elasto-plastic
244 constitutive model, fragmentation models, various equations of state (EoS), and multiple
245 materials (Melosh et al. 1992; Ivanov et al. 1997). More recent improvements include a
246 modified strength model (Collins et al. 2004) and the ε-α porosity compaction model
247 (Wünnemann et al. 2006; Collins et al. 2011). For natural materials like sand or sandstone, the
248 porosity compaction model has been tested and compared to mesoscale numerical models that
249 explicitly resolve pore space with high resolution, and to experimental data (Collins et al.
250 2011; Kowitz et al. 2013; Güldemeister et al. 2015; Wünnemann et al. 2016). At the
251 macroscale, the compaction model has been shown to give reasonable results in crater
252 (funnel) morphology and pore compaction (compacted funnel walls) up to very high
253 porosities (Luther et al. 2017).
254 Detailed comparison between model outputs and NASA Ames experimental data for
255 impacts into quartz sand from the 1970s have shown that the iSALE shock physics code can
256 accurately simulate the ejection process (Wünnemann et al. 2016). Also in large-scale
257 cratering processes, iSALE is capable of producing ejection data that agrees with observable
258 constraints as shown for the Orientale basin on the Moon, where the simulated ejecta deposit
259 (for different lunar thermal conditions) was compared with LOLA observations (Zhu et al.
260 2015; Zhu et al. 2017).
261 To study the effect of material properties on ejection characteristics, we use a single
262 impact scenario with invariant impactor parameters and Earth gravity. The spherical

projectile, 25 m in radius resolved by 20 cells, impacts with a velocity of 5 km/s, which corresponds to Π_2 of 3.2e-5. The pairs of Π_2 and Π_V in this study are given in Table A2.

For the simulation of the thermodynamic material behaviour, we use an analytic equation of state (ANEOS) of quartzite for both projectile and target (Melosh 2007). The yield strength of the projectile is neglected. For the strength of the target we use a Drucker-Prager rheology model. The strength model is described as:

$$Y = min(Y_0 + \beta\ P\ , Y_{max}) \tag{15}$$

with P being the pressure, Y_0 the cohesion, β the coefficient of friction, and Y_{max} maximum yield strength. Most of the models in this study consider a cohesionless (granular) material behaviour. We assume a range of the coefficient of friction from 0.0-1.0 for nonporous material as well as for a moderate porosity Φ=0.42. In addition, we investigate the effect of cohesion Y_0 in a range from 0-150 MPa, which shall mimic the behaviour of competent rock instead of granular material. However, we do not account for the fact that dynamic fracturing of the material will result in a significant weakening of (Collins et al. 2004). The limiting yield strength Y_{max} is set to 1 GPa. Thermal weakening was considered in the simulations using typical parameters for rock (Ohnaka 1995; Collins et al. 2004).

Besides strength, common target materials also differ in porosity. We therefore conducted a series of numerical experiments with cohesionless targets and porosity ranging from Φ=0 to Φ=0.42. For all those models where porosity was varied the coefficient of friction was set to 0.6. Apart from porosity itself, the parameters describing the porosity compaction behaviour were kept constant. Detailed values are given in the appendix. Note, some combinations of material properties do not reflect the behaviour of real materials. For example, a nonporous (Φ=0), cohesionless (Y_0=0) material is unrealistic as granular material always contain some porosity. Noncohesive (Y_0=0) and frictionless (β=0) material implies fluid behaviour of a dense rock, which also does not exist in nature without extreme heating. However, for a systematic study on the effect of material properties there is illustrative value in including such hypothetical end-member cases.

Ejection dynamics are expected to depend on the impact velocity. In general, faster projectiles are able to produce ejecta that are faster than for slower projectiles. To study this scenario, we run models with velocities between 1 km/s and 20 km/s and adapt the projectile size according to crater scaling relationships as shown in Eq. (3), yielding approximately the same crater volume for the different scenarios. We use a cohesionless, non-porous material

with a coefficient of friction of 0.6 for these simulations (for both target and impactor). The scaling exponent μ that is required to estimate the projectile size for a given impact velocity that results in the same crater size was taken from Prieur et al. (2017) and corresponds to 0.44.

We use a grid with 750 horizontal and 700 vertical cells. On the top, at the bottom, and on the side, 120 cells where the space increment increases gradually by 3% are added to ensure that the domain boundaries do not influence ejecta behaviour.

Previous studies have shown that iSALE and the material models above are suitable for modelling impact craters with a continuum approach where the material is advected in an Eulerian grid. However, to track the trajectory of ejected material requires knowledge of the history of each material parcel, which is not naturally recorded by an Eulerian code. Furthermore, accurate simulation of the ejecta curtain as it thins requires very high spatial resolution. Therefore, we use about 1000-10000 Lagrangian tracers that are distributed equally in the centre of each computational cell initially and that are moved with the velocity field of the material flow during the simulation. We record the horizontal and vertical velocity components (i.e. speed and ejection angle), launch position and launch time of the tracers at the point of time they are considered to be ejected. We define the time of ejection as the time when the tracer reaches the altitude of one projectile radius above the surface. This approach is simplistic, because it assumes that at this altitude the material represented by the tracer is moving ballistically (i.e., only influenced by gravity) and yet also travelling fast enough that gravity has had insufficient time to deflect its trajectory. An ejection altitude of one projectile radius is a compromise. If the criterion is set to a lower altitude, closer to the target surface, large variations in angle and velocity occur because pressure gradients are still influencing material motion; the ejecta is not yet moving ballistically. On the other hand, an ejection altitude criterion that is too high will lead to an underestimate of ejection angles (and potentially not capturing the ejecta entirely) for slow ejecta, expelled near the crater rim.

Although the simple criterion that we adopt excludes a small amount of material that does not reach a height of one projectile radius, which occurs near the rim towards the end of crater excavation, we find that it gives a relatively robust measurement of ejection speed and angle. We compared ejection statistics for several altitudes for this criterion and found a general consistency in the average ejection speed and angle for altitudes greater than about one projectile radius. While the spread in ejection angles is reduced at higher ejection altitudes, this also excludes more of the slower ejecta (see Appendix for more details). To derive the launch position for the ejecta at the surface level, we interpolate the launch position linearly to the target surface, based on the determined velocity vector. The mass of the ejected

material is assumed to equal the mass of material within the cell where each tracer originally is located before the impact.

In order to account for precise time stepping, which is crucial for a correct interpretation especially of the fastest ejecta close to the impact point, we use the described method above that has been recently implemented into iSALE to detect ejected tracers and record their ejection parameters. This implementation is not included in the standard iSALE Dellen distribution.

Based on the ejection characteristics, we calculate the final distribution of the ejected material under Earth gravity by analytically calculated parabolic trajectories. Hereby, we assume a flat target. From the mass of each tracer and a reference density of the ejected material as the initial density of the material, we calculate the volume of deposited ejecta. By radially binning the location of ejecta, we can calculate the surface area of each bin and thus, we can derive the thickness of the deposited ejecta in each bin. Typically, we use ~100 bins and consider ejecta up to a distance of ~200 projectile radii. Note, we neglect any ejecta sliding or modification to the target material by the falling ejecta (i.e. ballistic sedimentation or secondary mass wasting, Hörz et al. 1983). Early ejected material is fast and deposited at the largest radial distance. It can cause an outward material sliding and mixing of ejecta with local target material that alters the theoretical ejecta thickness to some extent. In addition, the formation of final craters by inward slumping material will change the ejecta deposit close to the transient crater rim. By assuming parabolic trajectories, we furthermore neglect effects of interaction with an atmosphere or vapour plume (Schultz 1992; Barnouin-Jha and Schultz 1996; Artemieva et al. 2013) and the effects of spatially varying gravity. This study focuses on effects caused by target properties only, and atmosphere induced changes in the ejecta distribution are subject to a future study. Hence, our results are directly applicable to small craters on planetary bodies without an atmosphere. For larger (i.e. complex) craters or basins with diameters of several hundred kilometres, care must be taken about the relation of transient to final crater radius when comparing to observational data and the planetary curvature. Large craters on Earth might be compared as long as ejecta masses are dense enough to show little perturbation by the atmosphere (valid for rather proximal ejecta).

COMPARISON TO EXPERIMENTAL DATA AND SCALING MODELS

In addition to previous validation studies (Wünnemann et al. 2016) we explicitly test our approach to determine the ejection characteristics against laboratory data. We compare two of our models that approximately reproduce the target properties of the materials used by Cintala et al. (1999), Anderson et al. (2004), and Housen and Holsapple (2011) in order to show that our model results fall into the same range, despite the very different impact scenarios (impactor mass and speed) considered. We use a coefficient of friction of 0.6 and a porosity between 30% and 42%, which we consider to be typical for the material (sand) used in the experiments. The real coefficient of friction was not stated in these studies. For comparison, we also show predicted behaviour from scaling relationships (Eq. (10)) for several target materials using parameters given by Housen and Holsapple (2011). The comparison is shown in Figure 2, where we plot launch velocity and ejection angles as a function of launch distance. Note that launch velocity and distance are normalised by the term $\sqrt{g\,R}$ and crater radius (Figure 2 (i) and (ii)), respectively. We use a different size-scale to the experimental data in our model because simulations of real experimental sizes are computationally expensive due to the high cratering efficiency (cf., Pierazzo et al. 2008). However, following the concept of scaling relationships, our comparison is justified as long as the scaling relationships hold true. The comparison shows that the model results are consistent with the predicted ejection velocity from Eq. (10): the velocity data plot in the expected range for the sand scaling relationship, especially for $x/R>0.5$. Even more pronounced is the agreement of our model data for velocity (Figure 2 (i)) and the experimental data from Cintala et al. (1999), Anderson et al. (2004), and Housen and Holsapple (2011).

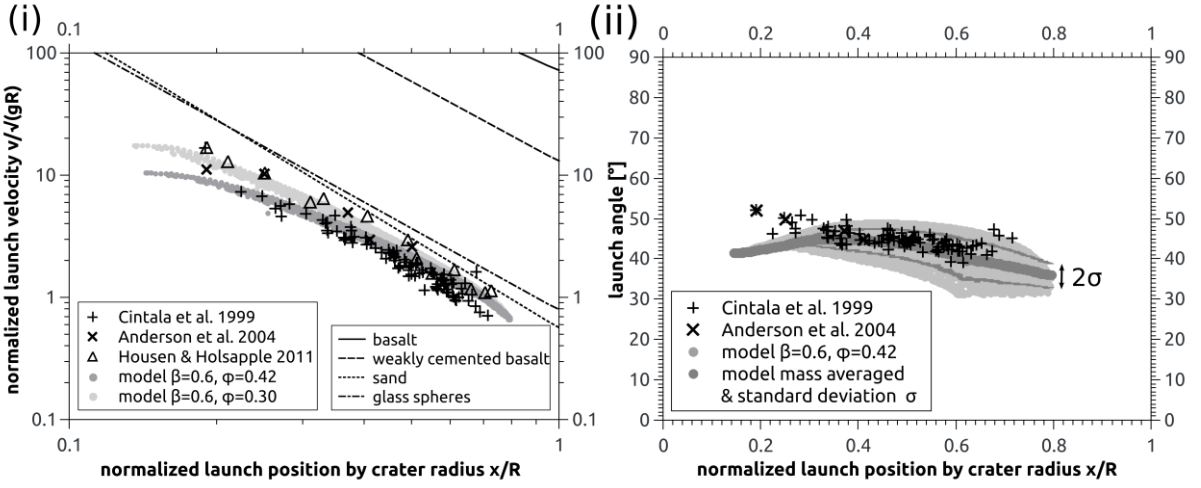

Figure 2: Ejection behaviour of cohesionless target materials with a coefficient of friction of 0.6 and a porosity of 30% (light grey symbols in (i); model represents dense sand as given by Housen and Holsapple 2011) and 42% (grey symbols; model represents coarse sand as given by Cintala et al. 1999). The porosity of the sand used by Anderson et al. (2004) is not further specified, but falls into the same range of porosity. The launch velocity is normalised by the term $\sqrt{g\,R}$ (i), ejection angles are given in degree (ii), and the distance is normalised by crater radius. In addition to our model data, we plot experimental data (cross symbols; Cintala et al. 1999 and Anderson et al. 2004; and triangles; Housen and Holsapple 2011) and the scaling relationships (Eq. (8) and (10)) for competent basalt, weakly cemented basalt, sand and glass spheres (solid, dashed, dotted and dash-dotted lines, respectively; see Housen and Holsapple (2011) and references therein). The crater size given by Cintala et al. (1999) was measured as rim-to-rim diameter and we estimated 10% difference to the apparent crater diameter. For basalt we arbitrarily assume R/a~20. The modelled impact velocity is 5 km/s. The simulated projectile radius is 25 m. Ejection angles are averaged with a mass weighted moving average with 100 data points. Cintala et al. (1999) used projectiles with a=2.38 mm and v_i=1.4 km/s, Anderson et al. (2004) used a=3.18 mm and v_i~1 km/s, and Housen and Holsapple (2011) used aluminium cylinders with a=6 mm and a height of 12 mm, and v_i=1.4 km/s.

The ejection angle taken from our model varies by about ~12° for a given launch distance for a sand-like target (light grey circles, Figure 2 (ii)). This is comparable to, but somewhat greater than, the ~8° spread in the experimentally determined ejection angle. This discrepancy might be because some fraction of ejected material might not have been captured by the experimental technique used, as acknowledged by Cintala et al. (1999). The experiments were designed to detect a wide range of ejection speeds, but had to exclude very fast or slow ejecta. Furthermore, it was difficult to detect very small particles (Cintala et al., (1999), state an optimum detection size range of ~1-3 mm). On the other hand the simplified criterion used to determine ejection angles in our models might exaggerate the ejection angle spread in the model data (see Appendix). As ejection angle distributions have not been determined experimentally for many materials, it is possible that some of this enhanced spread is real. For example, a certain spread may be expected to some extent because of the physics behind the ejection process. The detailed interaction between the shock wave and the free surface implies that material ejected from near the surface will experience a different combination of acceleration and deceleration vectors from the shock and release waves compared to material that is ejected from deeper within the target (e.g., Melosh 1985, cf. Figure 1). On the other hand, the spread might be exaggerated in the models compared with reality. One possible influencing factor is spatial resolution. At the time of ejection (when a tracer satisfies the criteria defined above) the ejecta curtain is typically only resolved by a

421 couple of cells. While the nodal velocity vectors across the curtain show a relatively
422 consistent speed, the angle of the vectors varies, which may result in the observed spread in
423 the angle data. Another factor is mass-weighting of the tracer data. In Figure 2 (ii) we show
424 modelling results in which each tracer (light grey circles) is treated equally. However, each
425 tracer actually represents a different mass depending on its radial position of origin. Very
426 proximal tracers represent a smaller mass than those that originate further away from the
427 symmetry axis due to the cylindrical geometry. To correct for this effect, we process our
428 simulated angle data in order to give some uncertainty range and to enable a mass-weighted
429 comparison between experimental and modelling data for the ejection angles. Given the fact
430 that different model data points represent a different mass, we show our results for ejection
431 angles as a moving mass weighted average with a mass weighted standard deviation. This
432 method allows for the determination of the range of angles where most of the material is
433 ejected. Figure 2 (ii, dark grey circles and lines) shows that the observed variations in ejection
434 angles fall into the envelop given by the standard deviation (~ $\pm$4°) from the mass-weighted
435 average. Also for targets with a large range of ejection angles for a given launch distance we
436 can reduce the spread in the raw data significantly. A deviation of speed and angle between
437 model and laboratory data for small launch positions $x/R<0.2$ might be related to the smaller
438 cratering efficiency of our scenario: a similar initial pattern of rising ejection angles at early
439 stages (close to the projectile) has been shown at least in some experiments by Hermalyn and
440 Schultz (2010).

441 # RESULTS

442 In this section, we present our model results for the effect of the coefficient of friction,
443 porosity, and cohesion on ejection velocity and angle. We normalise our results of ejection
444 velocity and launch position by impact velocity and projectile radius, respectively.
445
446 **Coefficient of friction:** In Figure 3 we show ejection velocities (i and iii) and ejection angles
447 (ii and iv) for models with coefficient of frictions between 0 and 1 for a non-porous case and a
448 42%-porosity case, respectively. An increase of the coefficient of friction does not change the
449 onset of material ejection or the velocity of the first ejected material for a given porosity.
450 However, farther away from the impact point, the material with the higher coefficient of
451 friction shows lower velocities and ejection ceases at shorter launch positions due to reduced
452 crater growth. This corresponds to a steepening of the slope in the double logarithmic

representation: e.g., at the relative launch position of 10 the velocities for the materials with the largest and lowest coefficient of friction differ by a factor of four.

For the smallest launch position, the angle of ejection depends on the coefficient of friction (Figure 3 (ii) and (iv)). After a short regime of steepening of the ejection angle for the lowest launch positions, a maximum quasi-plateau is reached. This plateau is most pronounced for the lowest coefficient of friction (~5° lower angles for $3<x/a<10$) and reduces to a small peak for the largest coefficients in the non-porous case that is followed by a quick decrease in ejection angle. Furthermore, the ejection angle spreads most for the lowest coefficient of friction (~48-70° at launch position 10 for the nonporous material) while the range narrows for larger coefficients of friction (~5° at launch position 5 for the non-porous material). As shown in Figure 1, material that originates from a position close to the surface experiences a larger ejection angle than the material that followed the excavation path within the growing cavity. Consequently, and due to the 2D cylindrically symmetric geometry of the setup, the tracer of the material originating from shallow depth and larger distance from the impact point corresponds to a larger mass. In addition, this figure also shows the earlier cessation of ejection for larger coefficients of friction, which is due to smaller crater sizes. Interestingly, we see a small increase in launch angles for larger launch positions ($x/a>10$) for material with a coefficient of friction of 0.0 – 0.2 and no porosity. However, this increase of launch angle occurs at launch positions between about $0.7R$ and $1.3R$, where R is the radius of the transient crater measured at the preimpact level. Launch positions outside the transient crater radius occur if material in the crater rim reaches the height of the ejection altitude criterion (one projectile radius). Although this material reaches the prerequisite height, our analysis does not ensure that it is moving ballistically and therefore this material may not represent ejected material. Fortunately, its effect on the distribution of ejecta landing on the surface as a function of distance is small, as shown in section “Ejecta deposits” further down.

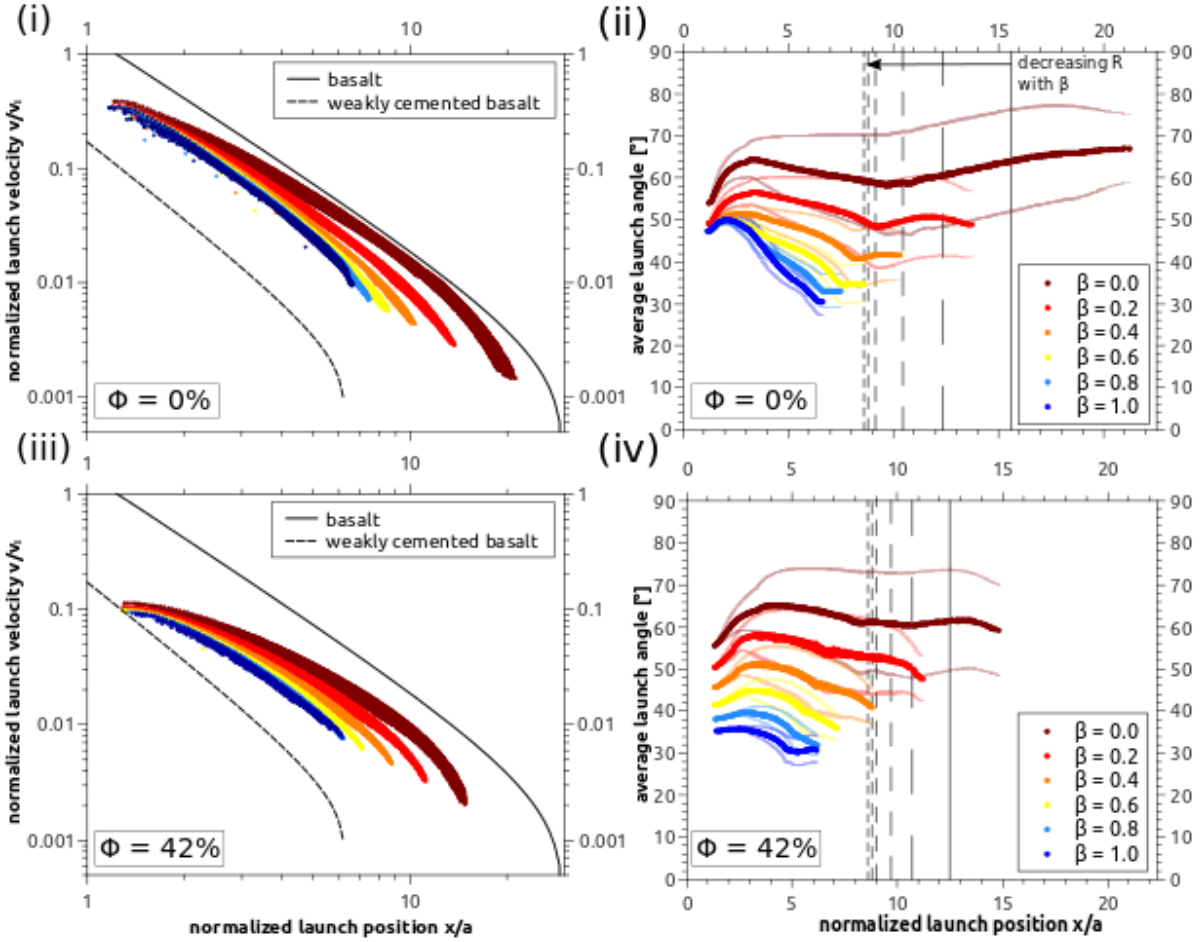

Figure 3: Launch velocity (i, iii) and launch angle (ii, iv) versus launch positions on the target surface. Target materials are cohesionless, nonporous (i, ii) or porous (iii, iv, Φ=0.42) and have different coefficients of friction. Velocity and launch position are normalised to the impact velocity and the projectile radius, respectively. The colour-scale corresponds to an increase in the coefficient of friction from dark-red to blue. In addition to our model data, we plot the scaling relationships (Eq. (8)) for competent basalt (equal scaling parameters as water) and weakly cemented basalt (solid and dashed lines, respectively; see Housen and Holsapple (2011) and references therein). For basalt we arbitrarily assume R/a~20. Note, that the velocity data for the highest coefficient of friction in (i) and (iii) overlaps with the other data. Ejection angles are averaged with a mass weighted moving average with 500 data points (ii, all β and iv, β = 0.0) and 100 data points (iv, all β > 0.0), respectively. The crater size is shown by the grey lines ((ii & iv), bold line to finely dashed line correspond to the scenarios with coefficients of friction of 0.0 to 1.0, respectively).

Porosity: Figure 4 shows ejection velocities (i) and ejection angles (ii) for models with porosity between 0% and 42% and a coefficient of friction of 0.6. An increase of the porosity substantially affects the velocity of the fastest ejecta at the same launch position (Figure 4 (i)). The fastest ejecta from the non-porous target material are ~3.5 times faster than the ones from

the material with 42% porosity. For more distal launch positions, the ejection velocities of the ejecta from the different materials align and ejection ceases at about the same distance. This corresponds to a flattening of the slope in the double logarithmic representation.

Ejection angles range from ~40° to ~50° for the different target porosities. However, the general slopes for the ejection angles of the different materials align well, including maximum angles that are reached for each model. Although visible only to some small extent, there seems to be a tendency for steepening of the ejection angle towards the highest porosities of 30% and 42%, while for 20% the average angle was the lowest for all materials.

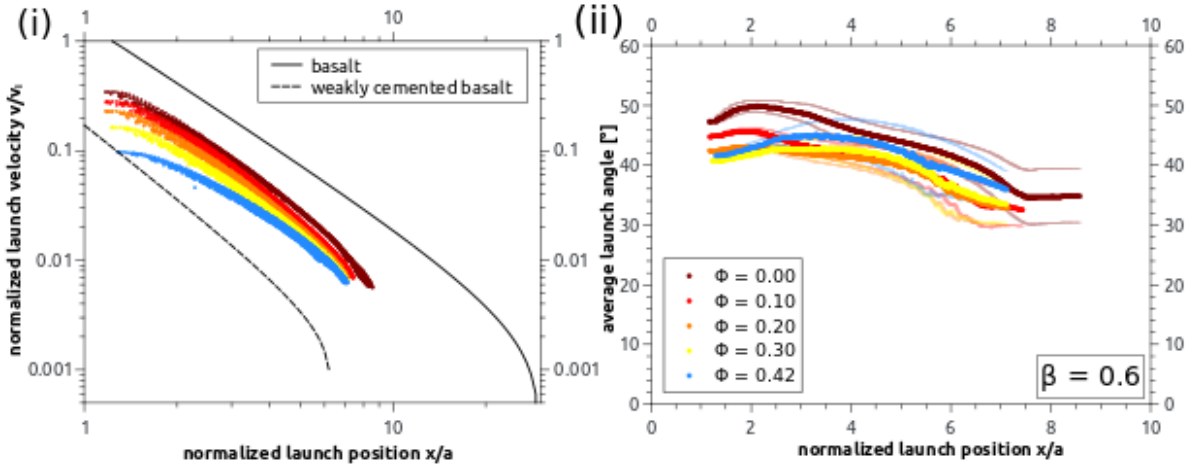

Figure 4: Launch velocity (i) and the launch angle (ii) versus launch positions on the target surface. Target materials are cohesionless, have a coefficient of friction of 0.6 and different target porosities. Velocity and launch position are normalised to the impact velocity and the projectile radius, respectively. The colour-scale corresponds to an increase in the coefficient of friction from dark-red to blue. In addition to our model data, we plot the scaling relationships (Eq. (8)) for competent basalt (equal scaling parameters as water) and weakly cemented basalt (solid and dashed lines, respectively; see Housen and Holsapple (2011) and references therein). For basalt we arbitrarily assume R/a~20. Note, that the data of ejection angles partly overlap. Ejection angles are averaged with a mass weighted moving average with 100 data points (ii).

Cohesion: In Figure 5 we show ejection velocities (i) and ejection angles (ii) for models with a non-porous material with a cohesion of 0-150 MPa and a coefficient of friction of 0.6. An increase of the cohesion of a material neither changes the velocity of the fastest ejecta at the early launch positions nor the slope in the double logarithmic representation (Figure 5 (i)). However, the cohesion affects the final size of the crater and thus the final launch positions of

the ejecta. An increase of cohesion leads to ejection velocities ceasing towards zero at smaller launch positions, which may correspond already to the rim.

Ejection angles for different cohesive material align well until the crater rim of each scenario, where ejection ceases. Increasing the cohesion does reduce the crater size and maximum launch positions. The early onset and the maximum ejection angle match for the different materials. The general range of angles agrees with the range resulting from different target porosities. However, material with the highest cohesion values is ejected at a narrow range of angles between 45°-50° and does not show the decline of ejection angle down to ~30° at the largest launch positions that seems to be typical for material with a substantial coefficient of friction.

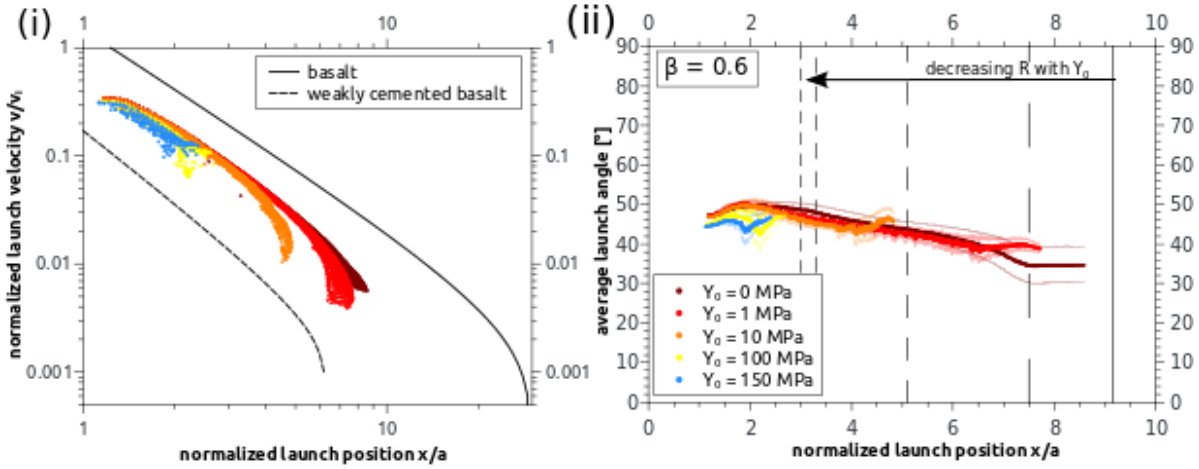

Figure 5: Launch velocity (i) and the launch angle (ii) versus launch positions on the target surface. Target materials are non-porous with different target cohesions Y_0 and a coefficient of friction of 0.6. Velocity and launch position are normalised to the impact velocity and the projectile radius, respectively. The colour-scale corresponds to an increase in the coefficient of friction from dark-red to blue. In addition to our model data, we plot the scaling relationships (Eq. (8)) for competent basalt (equal scaling parameters as water) and weakly cemented basalt (solid and dashed lines, respectively; see Housen and Holsapple (2011) and references therein). For basalt we arbitrarily assume R/a~20. Note, that the data of ejection angles partly overlap. Ejection angles for Y_0>0 Pa are averaged with a mass weighted moving average with 25 data points (ii); and for Y_0=0 Pa with 500 data points. The crater size is shown by the grey lines ((ii), bold line to finely dashed line correspond to the scenarios with 0 MPa to 150 MPa cohesion, respectively).

The common representation of ejection velocities and angles against launch positions normalised to projectile radii does not take into account the final crater size. As stated above, some differences we observe for ejection velocities are due to differences in transient crater

radii. Therefore, we also present the ejection velocity as a function of normalised launch positions relative to crater radius $\frac{x}{R}$ (Figure 6). For different coefficients of friction, we see an overlap of ejection velocities close to the crater rim for both non-porous and 42%-porous material (Figure 6 (i) and (ii)). Some slight differences occur in the non-porous case for very small launch positions. However, these differences (30-40 for x ~0.1) are smaller than differences that occur for varying target porosity (10-40 for x ~0.1, Figure 6 (iii)). Further differences can be found for velocity plots of different cohesion (Figure 6 (iv)). Here, we see an offset between the different scenarios that overlap in projectile normalisation. The cohesionless case plots in the range of the scaling relationship for sand, whereas the case with highest cohesion plots close to the scaling relationship of weakly cemented basalt that has a compressive strength of 680 kPa (Housen 1992). Note, that the normalisation used is typical for the gravity dominated regime. Larger cohesions will shift the scenario into the strength regime.

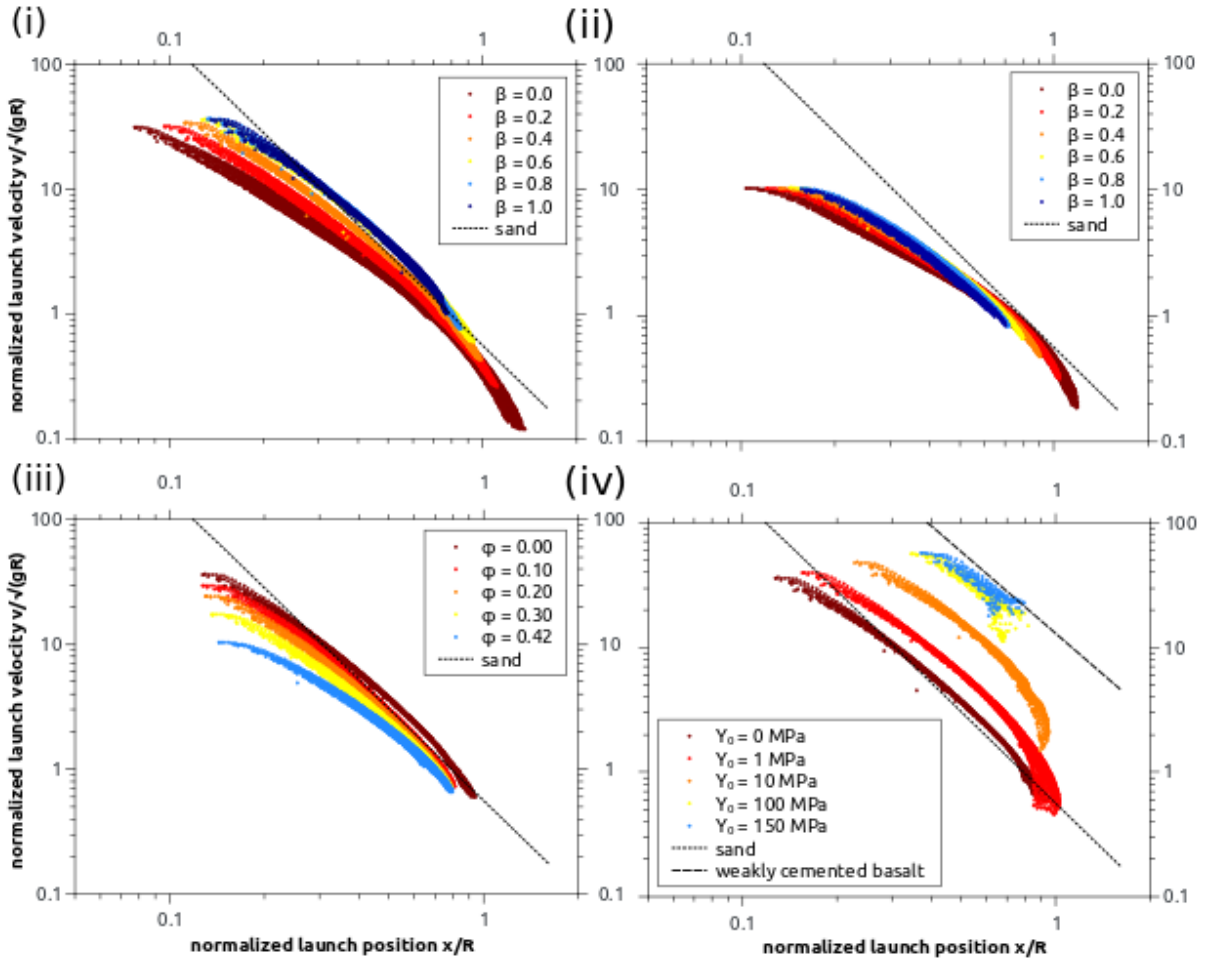

Figure 6: Ejection velocity for the same cases as shown in Figure 3 - Figure 5 ((i)-(iv), respectively). The distance is normalised to crater radius and the launch velocity to $\sqrt{g\,R}$. In addition to our model

data, we plot the scaling relationships (Eq. (10)) for weakly cemented basalt and sand (dashed and dotted lines, respectively; see Housen and Holsapple (2011) and references therein). In (i)-(iii), there is no cohesion. In (iii) and (iv), the coefficient of friction is 0.6.

Effects of impact velocity

In our study, we compare models with different impact velocities that result in the same crater size, as described in the method section (Table A2). In Figure 7, we show ejection velocities (i) and ejection angles (ii) for models with a non-porous material and a coefficient of friction of 0.6 for impact velocities in the range from 1 – 20 km/s. A comparison of these models shows that ejected material behaves similar for different impact velocities in terms of absolute launch velocities, but not in terms of ejection angles (Figure 7). In terms of ejection velocities, all models fall on the same line which is a consequence of the different projectile radii. The proximal ejecta of the slowest impact (= largest projectile) is launched at larger launch distance than in the scenario with 20 km/s impact velocity.

Differences are more pronounced for ejection angles: Keeping in mind the uncertainties in the measurement of ejection angles as discussed in the chapter "Comparison to experimental data and scaling models", lower impact velocities appear to result in lower ejection angles for our non-porous target. Thus, a larger fraction of the total momentum of ejected material goes in horizontal direction for lower impact velocities. Maximum ejection angles differ by a factor of about two comparing the fastest and the slowest impact. The most significant differences can be observed for locations close to the impact point (Figure 7 (ii)). Furthermore, we see that ejection angles for one launch position can vary more in the case of a fast impact than in the slower case. In contrast to the previous figures, we show the data in absolute values as the craters are about equal in size (< 8% difference of radius to reference value). Normalised plots are shown in the discussion section.

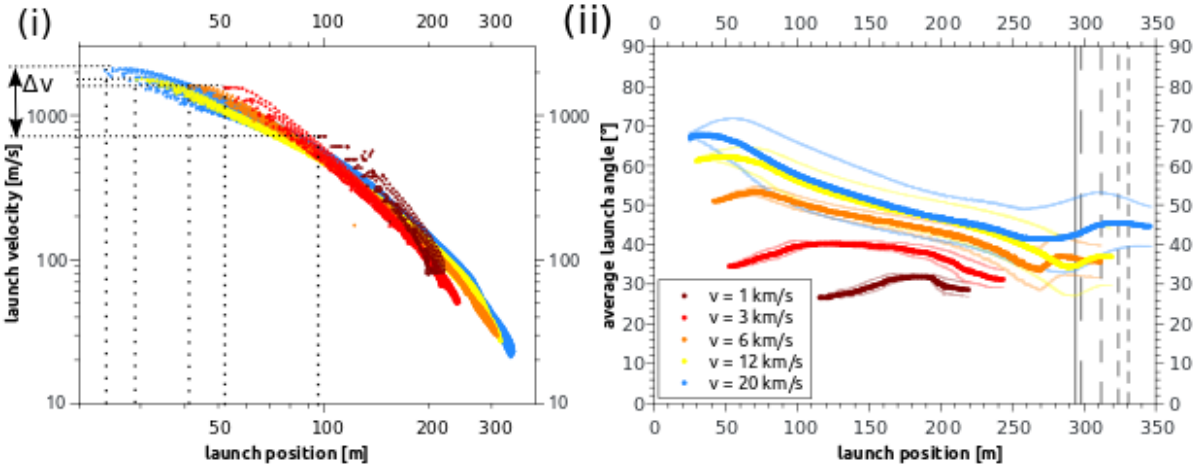

Figure 7: Absolute launch velocity (i) and the launch angle (ii) versus absolute launch positions on the target surface for different impact velocities. The target material is non-porous, cohesionless and has a coefficient of friction of 0.6. The colour-scale corresponds to an increase in impact velocity from dark-red to blue. Dashed and dotted lines show the projectile radii of the different models and the corresponding maximum ejection velocities, respectively. Ejection angles are averaged with a mass weighted moving average with 50, 100 and 500 data points for impact velocities of 1 km/s, 3-6 km/s, and 12-20 km/s, respectively (ii). The crater size is shown by the grey lines ((ii), bold line to finely dashed line correspond to the scenarios with an impact velocity of 1 km/s to 20 km/s, respectively).

Discussion

Effects of different impact velocities for constant crater size

In the previous results section, we show a comparison of ejection dynamics for different target properties, followed by a comparison of scenarios with different impact velocities. For a better understanding we begin our discussion with aspects for the latter cases as these serve as the best starting point of our argumentation. The results show that absolute ejection velocities for craters with similar volume follow the same trend for all impact velocities (Figure 7). For the averaged ejection angles, we see increasing launch angles at positions close to the impact point that agree with patterns described in previous studies of early excavation at similar launch positions to ours (Gulde et al. this issue; Hermalyn and Schultz 2010, 2011; Hermalyn et al. 2012). For slower impacts, ejection angles are shallower. These findings are not seen by Hermalyn and Schultz (2010) with 1.63 km/s as slowest impact velocity, but are in agreement with the trend observed by Hartmann (1985) for powdered basalt (5 m/s – 2.3 km/s). However, both studies used a different target material to the one we used for the velocity study, indicating that the effect is depending on the target

material used. The scenarios with an impact velocity of 6, 12 and 20 km/s are more similar to each other than the slower scenarios of 1 and 3 km/s impact velocity. The latter two velocities are smaller, or about equal, respectively, to the bulk sound speed in the target material (3684 m/s as derived by ANEOS for quartzite) and as such are not or only just in the hypervelocity regime and a shockwave-induced excavation flow may have not been fully established. Note that the speed of sound of the target material in the studies from Hartmann (1985) and Hermalyn and Schultz (2010) is substantially lower than for the non-porous target material we used for this velocity studies and, thus, the effects for low-velocity impacts that we see might occur at different velocities for other target materials. For such low-velocity impact scenarios crater formation and ejection of material mostly occurs in the nearfield, where the point source approximation to describe the excavation flow in the farfield is not applicable. Therefore, the scaling relation Eq. (3) used for the determination of the projectile parameters yielding the same crater volume does not hold true and crater mass and volume do not agree with the mass and volume of the faster scenarios (Figure 15). The ratio of maximum excavation depth to transient (maximum volume) crater radius (~0.2) is equal for all scenarios apart from the lowest impact velocity.

Although the ejection velocities for the scenarios with different impact velocities follow the same trend in absolute numbers, their trend diverges in the non-dimensional representation normalised to impact velocity and projectile radius (Figure 8 (i)) for launch positions $\frac{x}{a} \leq 3$. The maximum values at the smallest launch positions vary by about an order of magnitude between the 1 km/s and the 20 km/s scenario. The proximal slope is different for all models with different impact velocities. Only for larger distances the decay of the different models may agree. As the absolute velocities appear to be equal, the difference in the decay in the normalised representation is no surprise. Faster impacts correlate with smaller projectile radii if the same crater volume is reached (Figure 7). As such, the slope must flatten for faster impacts. Better agreement between the ejection velocities of the scenarios with different impact velocities can be achieved when plotting in crater parameter normalisation (Figure 8 (iii)). Apart from very early ejecta $\left(\frac{x}{R} < 0.2\right)$, the different models roughly plot on the same line, which corresponds to the line from sand scaling relationship (μ = 0.41). We will address this topic later on.

Larger differences appear in the ejection angles of the impacts with different impact velocity (Figure 8 (ii) and (iv)). The mass weighted average of the angles that we use suggests that for the fastest impacts, a larger fraction of the ejection velocity goes in a vertical direction whereas it is more in a horizontal component for the slower impacts. As mentioned before, the

654 excavation flow that is transferred onto the material by the shock wave initially has a radial
655 direction away from the source of the shock wave. The onset of the rarefaction wave causes a
656 pressure gradient, and thus adds an upward component to the excavation flow (Gault et al.
657 1968; Thomsen et al. 1979; Melosh 1989). In our scenario with different impact velocities,
658 peak pressures will increase with impact velocity whereas the isobaric core will be smaller
659 and probably shaped differently as the projectiles are smaller. We argue that the increase in
660 peak pressure with increasing impact velocity causes a larger pressure gradient that,
661 consequently, will add a larger upward component to the velocity field. Note that the effect of
662 varying impact velocities is less pronounced in more porous targets. For targets with a
663 porosity of Φ=0.42, ejection angles reach ~38° and ~45° for impact velocities of 1 km/s and 5
664 km/s, respectively, and as such differ less than in a non-porous target where ejection angles
665 reach ~30° and ~53° for impact velocities of 1 km/s and 6 km/s, respectively. Target
666 properties will be discussed further in the next chapter. Note further, that in early ejection
667 times an effect of projectile parameters (e.g. density) on initial launch angles was shown;
668 resulting in higher launch angles for denser projectiles (Hermalyn and Schultz 2011). This is
669 in agreement with the explanation of larger shock pressures above: A larger impedance
670 contrast between projectile and target due to the density increase in the projectile causes
671 higher shock pressures (cf. e.g. with a steeper Hugoniot in Fig. 10 from Ebert et al. 2017), and
672 presumably also affects the geometry of the isobaric core and, hence, radial directions to the
673 isobaric core.
674

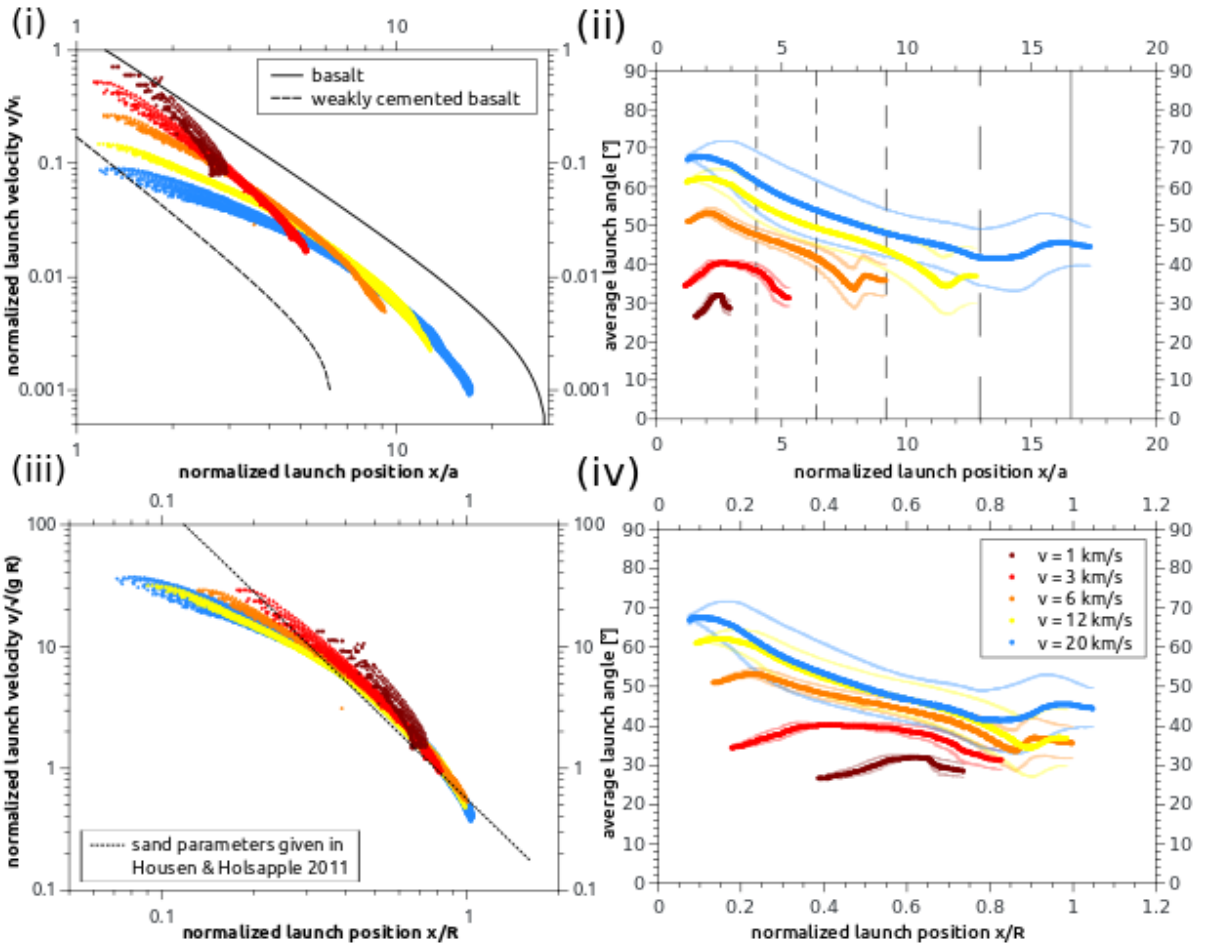

Figure 8: Ejection velocity and angle for the same cases as shown in Figure 7. The launch velocity is normalised to impact velocity (i) and $\sqrt{g\,R}$ (iii), respectively. The launch positions on the target surface are normalised to projectile radius (i & ii) or crater radius (iii & iv). In addition to our model data, we plot the scaling relationships (Eq. (8) and (10)) for competent basalt (equal scaling parameters as water), weakly cemented basalt, and sand (solid, dashed, and dotted lines, respectively; see Housen and Holsapple (2011) and references therein). For basalt we arbitrarily assume R/a~20. The colour-scale corresponds to an increase in impact velocity from dark-red to blue. Note, that the data of ejection angles partly overlap. Ejection angles are averaged with a mass weighted moving average with 50, 100 and 500 data points for impact velocities of 1 km/s, 3-6 km/s, and 12-20 km/s, respectively (ii & iv).

Target properties and excavation flow

In the following, we discuss the mechanism that causes the different ejection characteristics that we observe for different target properties. In the previous section, we discussed pressure gradients that differ due to the increased peak pressures with impact velocity, and different isobaric cores due to different projectile size. In our impact cases with varying target properties, we use equal impact conditions. Hence, the peak pressure and the

size of the isobaric core are similar (Figure 9), and peak pressures exceed the material strength, causing similar proximal $\left(\frac{x}{a} \leq 2\right)$ ejection velocities and ejection angles for different coefficients of friction in the non-porous case (Figure 3 (i) and (ii)). However, with increasing distance from the impact point we see more pronounced differences in the ejection characteristics that are caused by differences in the attenuation of the shock wave as a consequence of material properties such as strength and porosity (cf. decrease of peak pressure in Figure 10). In either case shock wave attenuation is enhanced because of energy dissipation by plastic work. Hence, the greater attenuation in pressure with distance in the target (Figure 9), leads to smaller pressure gradients in upwards direction. In addition, peak pressure isobars are shaped differently and the pressure gradient vector at shallow depths and at a given normalised radius points less-steeply towards the surface in the simulation with a larger coefficient of friction (Figure 9). Consequently, as friction coefficient is increased, the upward-directed acceleration is less and ejection angles shallower for launch positions $\frac{x}{a} \geq 2$ (Figure 3 (ii)). Experimental results for ejection angles for pumice and sand (the coefficient of friction of pumice is larger than for sand) support our conclusion (Hermalyn and Schultz 2014).

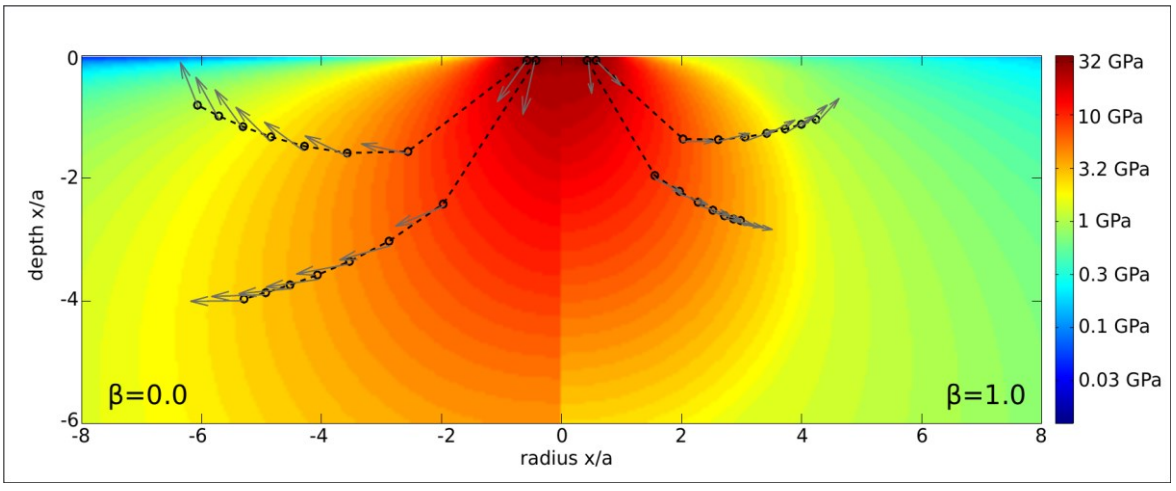

Figure 9: Peak pressure contours and gradients for two different coefficients of friction. The colour scale shows the peak pressure that was reached at the given location within the target for cohesionless, nonporous materials with coefficients of friction β=0.0 (left side) and β=1.0 (right side). Dashed lines indicate two exemplary tracer trajectories for equal initial positions. Grey arrows depict the direction of the gradient of peak pressures at the given locations.

When porosity is added to the target material, the behaviour of ejected material again changes (Figure 4). Very proximal ejection velocities are very different and converge only

towards the crater rim, whereas ejection angles do not differ much between the different scenarios (10° for the smallest launch positions). The decrease of maximum ejection velocities correlates with lower peak pressures in the target material with increasing porosity (Figure 10). As a result, the pressure gradients and acceleration from the shock wave decrease as well, causing the slight decrease in proximal ejection angles. However, for larger ejection distances, differences between the models disappear; so the same must hold true for pressure gradients in the target. Different processes due to the presence of porosity acting towards an increase (+) or decrease (-) of the ejection angle ((I) faster attenuation (-) and lower peak pressure (-) of the shock wave (Figure 10), (II) longer duration of the unloading path (+), (Güldemeister and Wünnemann 2017); and (III) enhanced thermal weakening due to pore space crushing (+), Wünnemann et al. 2008), respectively, balance out each other so that for different porosities the ejection angles remain constant. Note, that ejection angles for the largest porosity in parts are slightly larger than all other porosities, and especially larger than the nonporous scenario. Note further, that we discuss only porosities up to 42%. Cratering in very porous targets can lead to an almost complete suppression of the ejection of matter for large craters (above a threshold size) due to the dominant mechanism of pore compaction and when cratering is dominated by the crushing strength (e.g. Housen and Holsapple 2012).

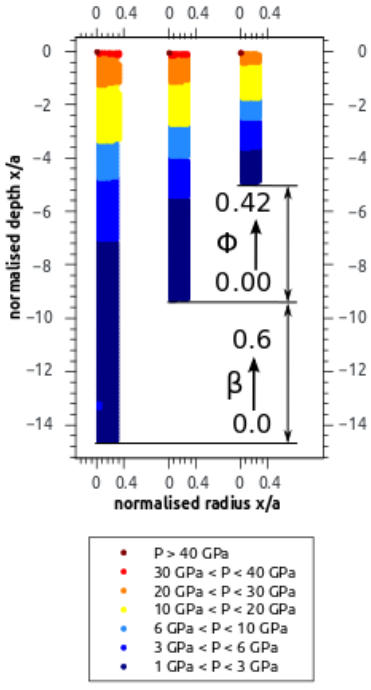

Figure 10: Peak pressure contours for three different materials. The colour scale shows the peak pressure range that was reached at the given depth within the target underneath the impact point. All

materials are cohesionless. From left to right, first the coefficient of friction increases from 0.0 to 0.6, and second porosity increases from 0% to 42%.

Implications for ejecta scaling

In this section, we discuss our results in the context of the scaling relationships shown in the chapter "Theoretical Background". One approach is to fit Eq. (7) to the model data in the normalisation to projectile size and impact velocity. However, for models with equal crater volume but different impactor parameters it was not possible to adopt a consistent range in launch position when normalised by impactor radius for fitting Eq. (7) to the data (Figure 8 (i)). The slope in the range $\frac{x}{a} \leq 3$ differs a lot for the different impact velocites. Therefore, we fit Eq. (10) to the model results in the normalisation to crater radius (cf. Figure 6 and Figure 8).

For fitting Eq. (10), we adopted a fixed criterion for the maximum launch position for the fitting range in order to achieve consistency in our results (given in Table A2). We define the maximum fitting range by a common minimum velocity of ~80 m/s for all models. Defining the maximum range in this way avoids including data too close to the rim, which may be affected by our ejecta selection criterion. For non-porous, cohesionless material, we find a nearly constant scaling exponent of μ = 0.46 - 0.49 and an increasing constant K_3 from 0.43 to 0.82 for coefficients of friction between 0 and 1 (Figure 11 (i)). The same trend of μ is observed for a material with 42% porosity. When increasing porosity from 0 to 42% for a constant coefficient of friction of 0.6, we find an increase in μ from 0.46 to 0.62, whereas K_3 first decreases from 0.77 to 0.60, before it rises again to 0.70 (Figure 11 (ii)). Increasing the cohesion for a non-porous material strongly increases μ as well as K_3 (Figure 11 (iii)). For increasing impact velocity from 1 km/s to 6 km/s for a cohesionless, non-porous target with a coefficient of friction of 0.6, we find an increase of μ and K_3 from 0.32 to 0.48 and from 0.59 to 0.85, respectively (Figure 11 (iv)). For larger velocities, these values remain constant. Note that this trend is inverse to the trend found by Yamamoto et al. (2017) for porous sand targets. However, this trend is similar to the one shown by Schultz (1988).

Literature values for sand like targets give a value for the scaling exponent of μ =0.41 (Housen and Holsapple 2011). Our closest results to these values have been achieved for non-porous, cohesionless materials with a coefficient of friction of 0.6 at an impact velocity of 3 km/s. However, sand has a significant amount of porosity, so that the corresponding simulated material should have porosity, as well. If we increase porosity, μ increases up to 0.62 for 42% porosity. This value is a bit larger than the value for rock like material or water (rock and

774 water: μ=0.55, Housen and Holsapple 2011), and much larger than the literature value for
775 sand of 0.41 that is based on crater size scaling. However, experimental measurements of
776 ejection dynamics for sand-like materials have shown the same discrepancy between μ-values
777 derived from crater scaling and ejecta scaling that we observed: Cintala et al. (1999) fitted
778 scaling relationships (Eq. (10)) to their ejecta velocity data and found values between 0.5 and
779 0.66. They attributed the discrepancy to the coarseness of their particulate target material
780 relative to the projectile size used. However, similar results were derived for finer-grained
781 sand targets in more recent experiments using the same technique for measuring ejection
782 velocity (Anderson et al. 2007). Similarly, Tsujido et al. (2015) find some deviation of μ
783 derived from crater scaling and from ejecta scaling with a scatter in the range of the data from
784 Cintala et al. (1999) in a study with different projectile densities at an impact velocity of ~200
785 m/s. Anderson et al. (2007) also mention some (partly unpublished) results where both scaling
786 results agree with each other. More recently, (Yamamoto et al. 2017) described a different
787 study that compared μ-values estimated from measurements of crater growth as a function of
788 time and crater size measurements that revealed a similar discrepancy in the scaling exponent
789 derived from both measurements. These studies of crater growth, excavation and material
790 ejection show differences in scaling relations for dynamic aspects of the cratering process that
791 involve both intermediate- and far-field phenomena versus singular, far-field observations
792 (e.g. crater size). One interpretation of such discrepancies is that the point source assumption
793 is valid for crater size, which is a metric dominated by far-field phenomena, but is not
794 satisfied for the dynamic aspects of cratering. Anderson et al. (2004) introduced the concept
795 of a moving flow field centre and argued that a stationary point source is not adequate for the
796 dynamic aspects of cratering. An implication of this result is that a scaling exponent derived
797 from crater sizes may predict incorrect ejecta behaviour when used in an ejecta scaling
798 relationship. It is therefore prudent to use scaling exponents derived for the process of
799 interest. It is likely that for impacts with large cratering efficiencies (i.e. small π_2), the point
800 source approximation might be more applicable also for describing dynamic aspects because
801 most of the excavation occurs more distant from the impact centre. Our findings for our
802 fastest impact velocities (12 km/s and 20 km/s, π_2=5.5 10^{-6} and 1.6 10^{-6} , respectively) show a
803 constant scaling exponent of μ =0.52, a value that is close to predicted values for non-porous
804 targets (rock and water: μ=0.55, Housen and Holsapple 2011), but still deviates somewhat
805 from crater size scaling results for similar numerical materials (μ=0.45, Prieur et al. 2017).
806

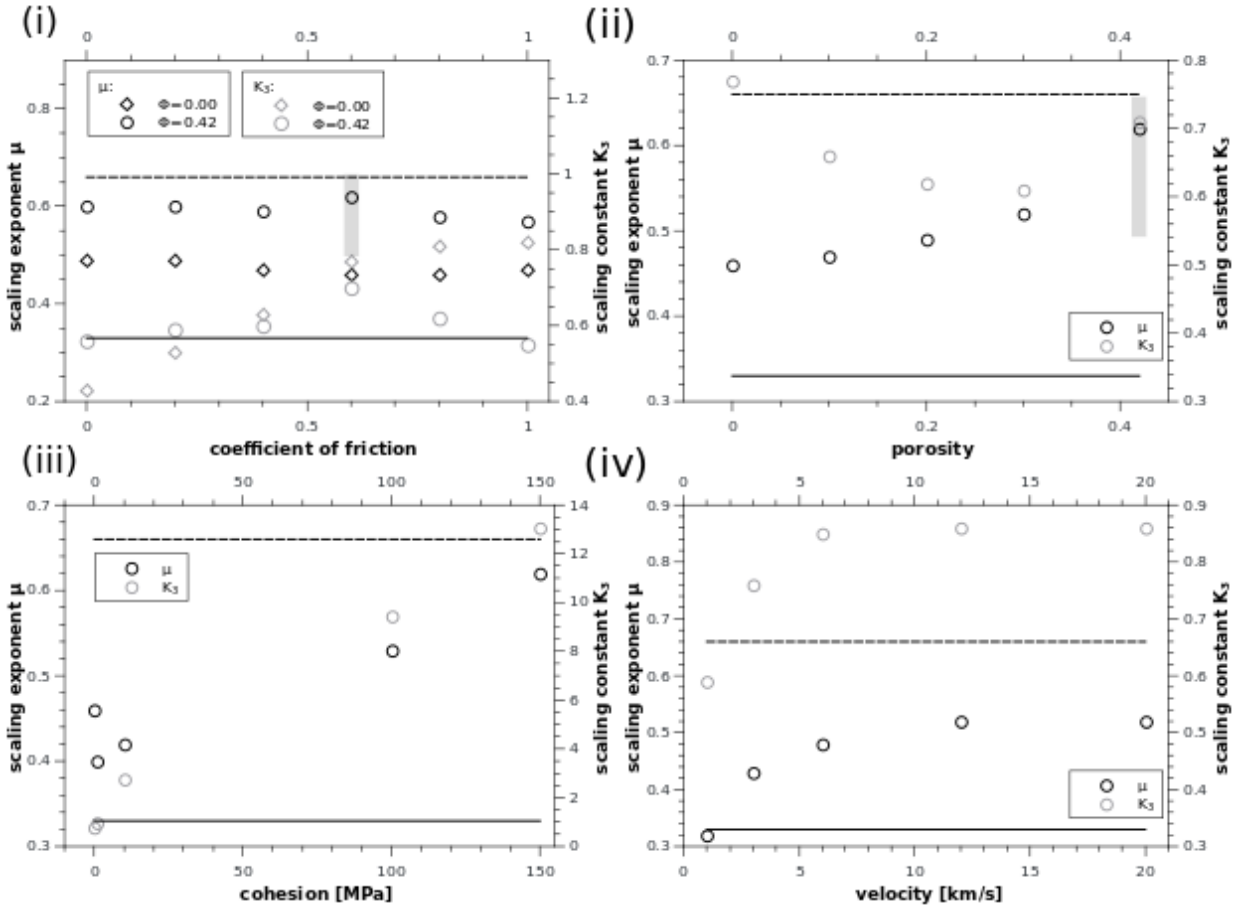

Figure 11: Ejecta velocity fitting results. Black symbols denote the scaling exponent, grey symbols the scaling constant. The results are given for the models shown in Table A2: (i) cohesionless target with Φ=0.00 (◊) and Φ=0.42 (o), (ii) cohesionless target with β=0.6, (iii) non-porous target with β=0.6, and (iv) a cohesionless, non-porous target with β=0.6. The black solid and dashed lines represent the momentum and energy scaling limits, respectively. The grey area depicts the range for the scaling exponent μ as derived by (Cintala et al. 1999) and most of the range from (Tsujido et al. 2015).

Ejecta deposits

We calculate the deposition of the ejected material based on the assumption of parabolic trajectories for the cases of different target materials mentioned so far. We do not consider any late stage modification processes, but show the amount of material that lands at a given radial distance. Our calculation takes into account the launch position of ejecta within the crater when calculating its deposition position. As a result, unlike the simple scaling model (Eq. (12)) the model-derived ejecta thickness distributions do not suffer from inaccuracies near the crater rim. We plot the thickness of the deposited ejecta against the radial distance normalised by the transient crater radius (Figure 12). For the scenario of a non-porous material (Figure 12 (i)) we see a decrease in the slope of the thickness of the deposited

ejecta for increasing coefficients of friction. The difference in ejecta thickness is most prominent in the proximal range $\left(\frac{x}{R} \leq \sim 3\right)$. For the same coefficients of friction, this effect is even more pronounced for the porous material with a porosity of 42% in a range until x< ~6 (Figure 12 (ii)). In contrast, little variation in the slope of the ejecta thickness is found for different target porosities with a constant coefficient of friction of 0.6 and ejecta thickness are nearly identical (Figure 12 (iii)). Only the nonporous case shows a thicker ejecta thickness that is about twice as thick as those of the porous materials for equal normalised distance x/R. The differences that result from cohesion are more prominent. Increasing cohesion results in a decrease of the slope of the ejecta thickness and in a reduction of its thickness. For the two largest values of a cohesion of 100 MPa and 150 MPa, only small thicknesses of the deposited ejecta are observed.

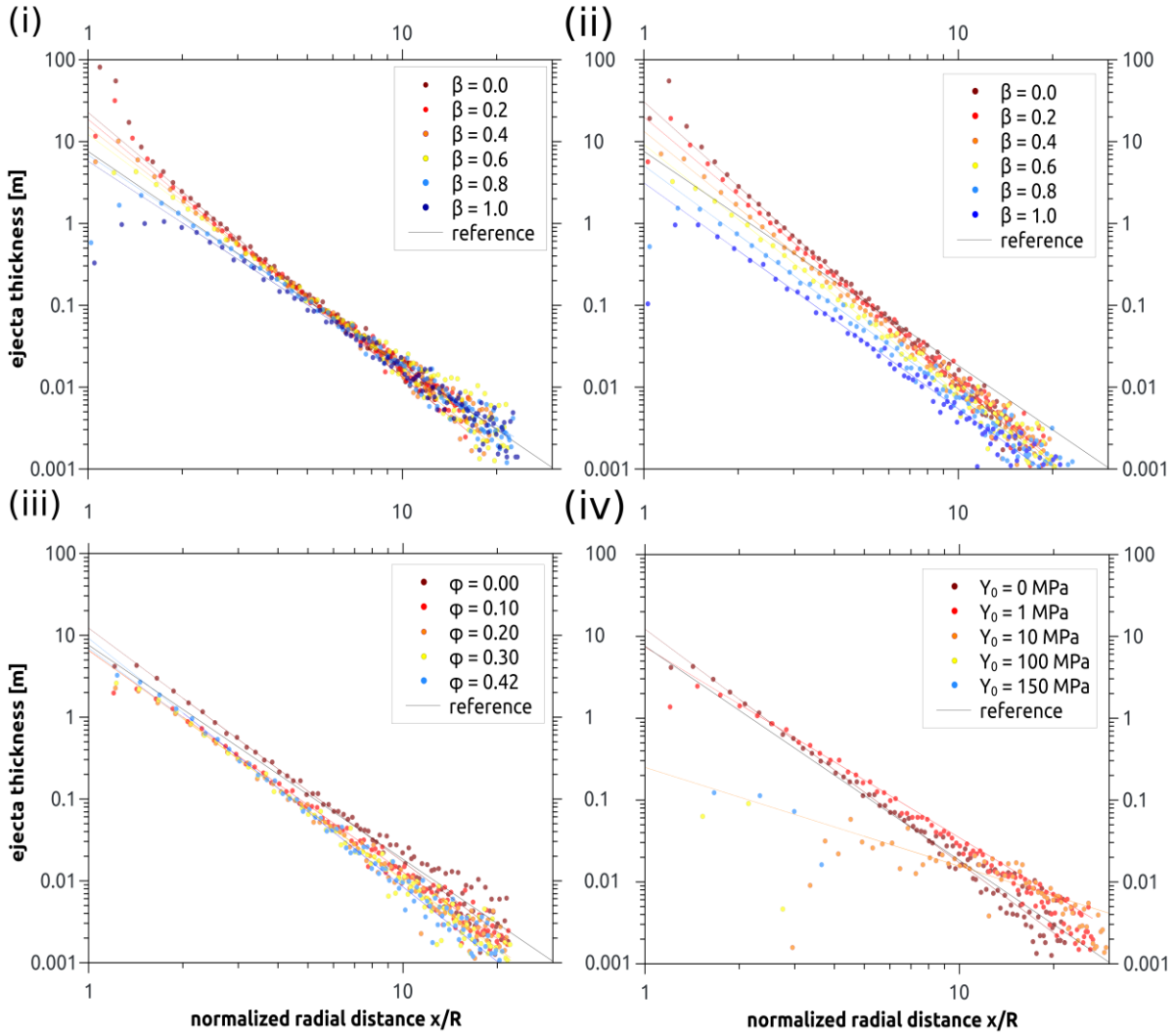

Figure 12: Distribution of the ejecta thickness for different target properties. The cases shown refer to: i and ii) different coefficients of friction in a nonporous and a porous (Φ=0.42) material, respectively

(cf. Figure 3), iii) different porosities (cf. Figure 4), and iv) different values of cohesion (cf. Figure 5). The distance is normalised to transient crater radii. For comparison with our results, we also show scaling data using Eq. (12) as a reference. We use a constant K_4 = 0.32 as given by Housen et al. (1983) and a sand like value of μ=0.41. We use a typical constant value of 45° as ejection angle. As reference crater radius we use the transient radius R=242.5 m of our model with 42% porosity and a coefficient of friction of 0.4. Note that the reference line assumes all ejecta emanates from the crater centre and, thus, is not expected to hold in the vicinity of the crater rim. In (i)-(iii), there is no cohesion. In (iii) and (iv), the coefficient of friction is 0.6.

Our results for different targets show that the effect of material properties on the ejection characteristics results in deviating ejecta trajectories and, thus, in different deposition thickness as a function of distance. Especially, the coefficient of friction affects the decay exponent of the ejecta deposit due to increasing ejection angles for lower friction values. Ejection angle close to 45° result in the furthest distances that the ejected material can reach. For the nonporous material that is the case for a coefficient of friction between 0.4 and 0.6. Lower coefficients of friction yield angles >45° resulting in ejecta accumulation close to the crater rim, as shown in Figure 12 (i). In contrast, for different material porosities ejection angles lie between 40° and 50° for a large range of launch positions. As such, the resulting ejecta deposits are similar in terms of decay exponent and ejecta thickness if distance is normalised by the transient crater radius (Figure 12 (ii)). The difference in ejection velocities that is affecting ejecta deposition is accounted for by the normalisation to the crater radius (that itself depends on the various porosities).

To support our previous statements, we fit the thickness of ejecta deposits over the radial distance with Eq. (13). We exclude data in the range $1 < x/R < 2$ from the fitting as a simple power law relationship is not expected this close to the crater rim, as evidenced by the simulation results. The different parameters for different target properties are given in Table A2, and are shown in Figure 13. The relationship between ejection angle and ejecta deposition mentioned above is shown e.g. by the larger T_0 for targets with low coefficient of friction (Figure 13 (i)). Furthermore, parameters for different porous materials remain nearly constant (Figure 13 (ii)). The smallest and largest exponents that we found give a range for B between 2.52 and 3.43 for the cohesionless targets. We also calculated the scaling parameter μ according to Eq. (14). However, we find that these values partly exceed the theoretical limit of energy scaling (0.66) and all models with porosity do not fall into the typical range of μ~0.4. One explanation for these results can be seen in too strong assumptions made for deriving Eq. (12), including one ejection angle instead of a range of angles, and the

negligence of exact launch positions. Furthermore, as indicated in the previous chapter, the static point source seems to have limitations for describing the dynamic aspects of cratering (e.g. material ejection). For deriving Eq. (12), dynamic and static aspects are combined, but only one scaling exponent (which has been shown to be not identical for both aspects of cratering in the previous chapter, or e.g. by Cintala et al., (1999)) is present in Eq. (12). Hence, the resulting scaling exponents from ejecta deposits should be considered with care. Consequently, comparing the derived scaling exponents based on the ejecta deposit with those derived by the velocity data, we find large differences in μ for 11 of 21 cases and only 6 cases where both results agree (Table A2). For the usage of scaling relations for ejection processes, we prefer the usage of the results based on the velocity plots instead of the deposits. For the μ derived from deposit data, we see a trend to smaller μ for increasing β. This seems to be so far reasonable as the scaling parameter for water is larger than the one for sand (0.55 and 0.41, respectively, Housen and Holsapple 2011).

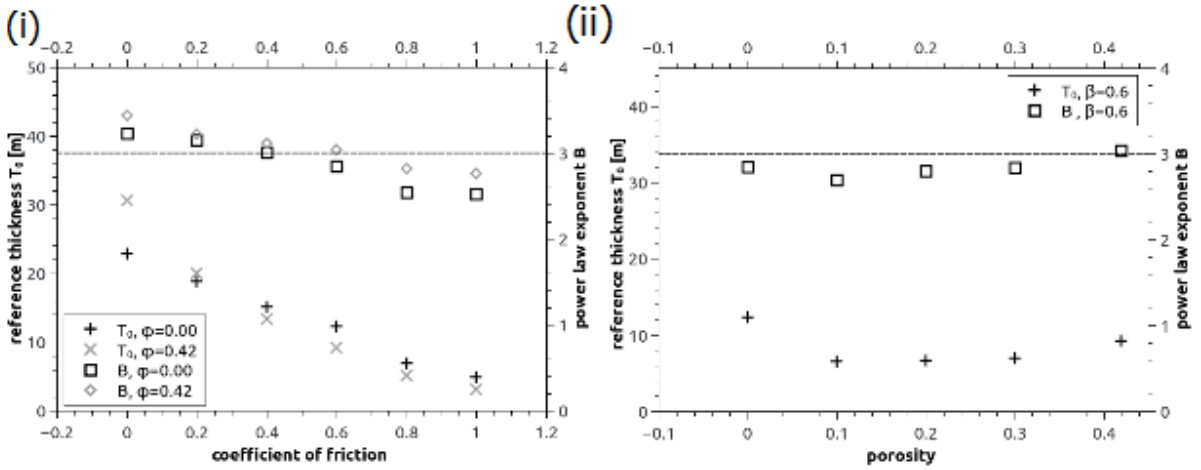

Figure 13: Ejecta deposit fitting results. In panel i), fit parameters are shown for different coefficients of friction for nonporous (black symbols) and 42% porous (grey symbols) targets. In panel ii), the same parameters are shown for different target porosities and a coefficient of friction of 0.6. All targets are cohesionless. The black dashed line shows the estimate of B=3 for large lunar craters (McGetchin et al. 1973).

Finally, we also studied different values of material cohesion for nonporous targets. We find that cohesion strongly reduces the amount of ejected material. Increasing the cohesion does not only reduce crater size, it also hinders ejection of lower velocity material by dominating the material strength after the passage of the shock and rarefaction waves (compare Eq. (15)). Accordingly, T_0 decreases. In addition, also B decreases with increasing cohesion.

We also modelled the ejecta thickness as a function of range for the scenario of different impact velocities (Figure 14) and a nonporous, cohesionless target with a coefficient of friction of 0.6. In this case, we observe a similar slope for all the ejecta thicknesses of different impact velocities, apart for the slowest case with 1 km/s that shows a somewhat flattened ejecta thickness. For the scenario with 3 km/s impact velocity, the slope is slightly lower than for the faster cases. The ejecta thickness in the proximal range $\left(\frac{x}{R} \leq 3\right)$ is equal for the cases with 6 km/s, 12 km/s and 20 km/s impact velocity. Those three scenarios also agree well in the total amount of ejected material as well as the total crater material (Figure 15). We calculated the crater mass based on the volume and the quartzite density of 2650 kg/m³. The slowest case of 1 km/s impact velocity shows a large deviation in both ejected and crater mass. The ratio of ejected to crater mass is ~0.37 and equal for the four fastest impacts. Only the 1 km/s shows a deviation also in this value (0.25).

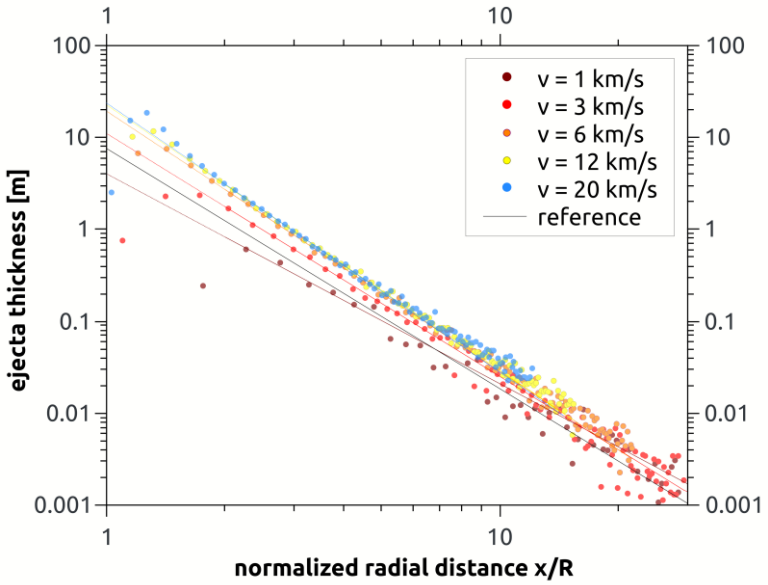

Figure 14: Distribution of the ejecta thickness for a nonporous, cohesionless target with different impact velocities. The cases shown refer to the ones in Figure 7. The colour-scale corresponds to an increase in impact velocity from dark-red to blue. For comparison with our results, we also show scaling data using Eq. (12) as a reference. We use a constant $K_4 = 0.32$ as given by Housen et al. (1983) and a sand like value of μ=0.41. We use a typical constant value of 45° as ejection angle. As reference crater radius we use the transient radius R=242.5 m of our model with 42% porosity and a coefficient of friction of 0.4. Note that the reference line assumes all ejecta emanates from the crater centre and, thus, is not expected to hold in the vicinity of the crater rim.

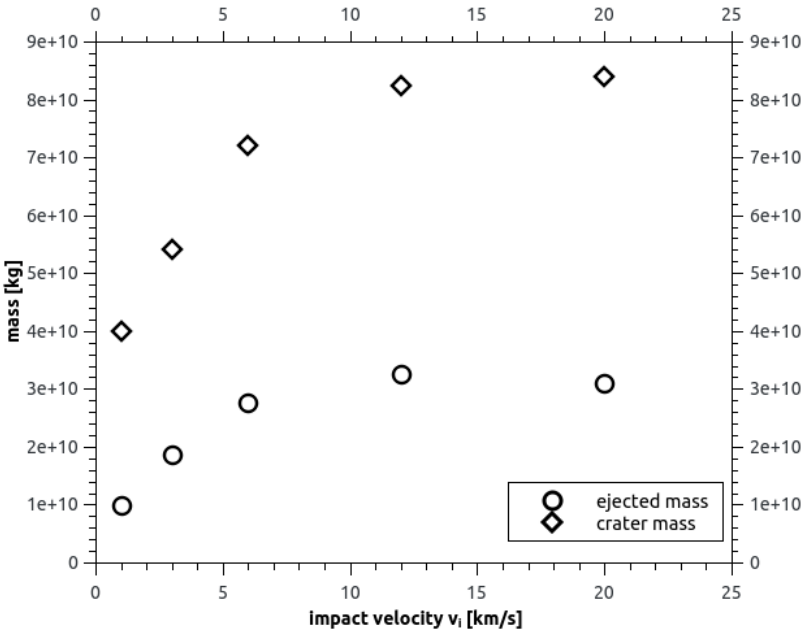

Figure 15: Crater and ejected mass for the cases of different impact velocities. For comparison, we considered only ejected masses with a velocity of at least 50 m/s. The ratio of both masses is ~0.37, excluding only the slowest impact with a ratio of 0.25.

For planetary applications it is interesting to see if there is a correlation between impact velocity and the distribution of the ejecta thickness. Again, we fit Eq. (13) to the data shown in Figure 14 for impact velocities between 1 – 20 km/s. The fitting parameters T_0 and B are plotted against velocity in Figure 16 and are listed in Table A2. The decay exponent of the ejecta thickness varies only slightly for all impact velocities. Only for the lowest impact velocity of 1 km/s we found a somewhat smaller decay exponent, which could be explained by the fact that such a low velocity does not represent hypervelocity-regime anymore. In general, the decay exponent does not allow for a distinction of (especially higher) impact velocities. Furthermore, no trend towards different thickness T_0 at the rim with increasing velocity can be observed. From 6 km/s to 20 km/s T_0 remains nearly constant. Also the ejected mass is nearly constant for these cases (Figure 15) as crater size was kept constant. Neglecting any post-deposition changes, it appears to be impossible to derive information on the projectile velocity by the ejecta thickness. Similar findings for the decay exponent have been shown for simulations of Orientale-sized impacts on the Moon by Zhu et al. (2015) for a projectile with 80 km diameter and impact velocities between 15 and 19 km/s. However, their ejecta thickness at the rim shows a slight increase with increasing impact velocity, i.e. larger coupling parameter (see Eq. (1)).

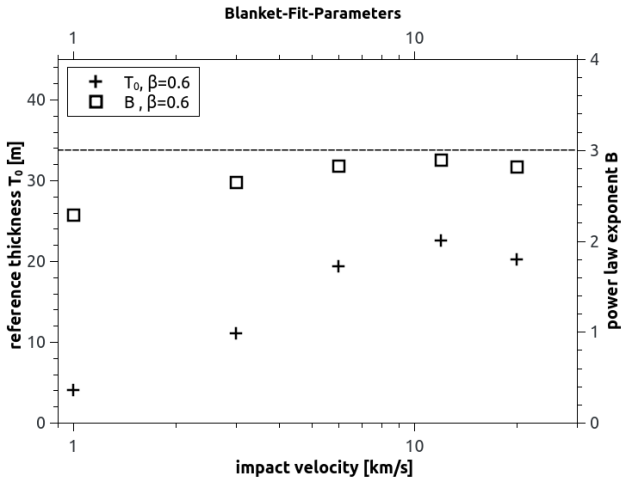

Figure 16: Ejecta deposit fitting results. The fit parameters are shown for scenarios with different impact velocity for non-porous targets with a coefficient of friction of 0.6. The target is cohesionless. The black dashed line shows the estimate of B=3 for large lunar craters (McGetchin et al. 1973).

Ejecta deposits at natural impact craters

According to our models the power law decrease of the ejecta thickness with distance, parameterised by the decay exponent B in Eq. (13) only depends on the coefficient of friction and cohesion, and is independent from porosity or impact velocity. From the study of lunar ejecta blankets, McGetchin et al. (1973) determined an exponent B = 3, and we find similar values of B for Earth gravity. Eq. (12) shows that the thickness of the deposited ejecta for gravity dominated craters does not depend on gravity. Hence, ejecta blankets on different planetary bodies have been found to be geometrically similar (Housen et al. 1983; Melosh 1989), and we can compare our results with ejecta blankets on bodies with different gravity.

The assumption that the scaling decay exponent μ depends only on material properties may allow for an inverse approach to determine material properties of the target from a given ejecta distribution. Fassett et al. (2011) determined the ejecta distribution of the Orientale crater and found a decay exponent of 2.8 ± 0.5. According to our models, this average value would correspond to e.g. a coefficient of friction of about 0.6 assuming a low porosity. Zhu et al. (2015), who use the ejecta distribution as a model constraint, use a similar coefficient of friction for the strength parametrisation of their heavily damaged material (note that they employ a more complex strength model). The ejecta distribution from their best fit model follows a decay exponent of 3.2; a value that we derive using a coefficient of friction of ~ 0.2. However, Zhu et al. (2015) account for thermal weakening of material due to a significant temperature increase with depth for the given scale of the basin structure, which would

974 explain the relative low strength (low coefficient of friction, low cohesion, Table A2) as our
975 study predicts.
976 On Earth, a comparison is possible to e.g. the Ries crater. Hörz et al. (1983) gave a
977 detailed description on the ejecta blanket (Bunte Breccia) and analyse possible ejection flows.
978 They give a decay exponent between 2.5 and 4, with 3 as a reasonable value. This range, of
979 course, is too large to distinguish between target properties. However, Hörz et al. (1983) state
980 that most of the material in the ejecta blanket originates from shallow target areas and, thus,
981 can show very similar target properties. Assuming that the simplistic approach of a Drucker-
982 Prager yield strength does describe this shallow material, we find an decay exponent of 4 to
983 be unrealistically high based on target properties, as it is an even larger value than for a 42%
984 porous, low coefficient of friction material. Lower values seem more realistic, with B=3
985 corresponding to a friction between 0.4 and 0.6 for a nonporous, noncohesive target and
986 B=2.5 corresponding to either an even larger friction up to 1.0 or additional cohesion. Note
987 that the range of coefficient of friction from 0.4-0.6 is in excellent agreement with the
988 coefficient of friction for sediments and basement material used by Collins et al. (2008) for
989 modelling the Ries crater. However, a comparison with the Ries crater is difficult and we
990 expect a deviation from our results from the parabolic trajectories due to the presence of an
991 atmosphere. Numerical results for ejection from small craters with the presence of an
992 atmosphere have shown differences in the thickness of deposited ejecta and show a reduced
993 range of the blanket (Shuvalov and Dypvik 2013). Furthermore, different authors (e.g.
994 Hüttner 1969; Oberbeck 1975; Hörz et al. 1983) demonstrated the importance of the
995 contribution from local material during the ejecta emplacement.
996 In very small scale, we can compare our results to laboratory data. Stöffler et al.
997 (1975) conducted impact experiments into sand and measured the ejecta distribution
998 thereafter. They find a decay exponent of 3.2. This value corresponds to a coefficient of
999 friction between 0.2 and 0.4 for the given porosity of 42%. Even though Stöffler et al. (1975)
1000 did not determine the coefficient of friction of the sand used, 0.4 seems a reasonable value.
1001 Based on the previous discussions, it is possible that detailed measurement of ejecta
1002 blankets from observations and laboratory experiments might reveal properties of the target
1003 material or even the thermal structure of the target at the time of the impact (cf. Zhu et al.
1004 2017). However, further laboratory and modelling studies on this topic are needed to test this
1005 hypothesis including varying thermal profiles and using more complex rheological target
1006 setups. There are certainly several limitations of our analysis that may hinder attempts to
1007 derive information about the target at the time of impact from ejecta deposits. In addition, the

comparisons made so far by this approach do not include modification processes. We do not account for crater modification in the case of complex craters. In this case, modification of the transient crater would cause slumping of material into the crater, resulting in a final crater that is larger than the transient crater (summarised recently e.g. by Krüger et al. 2017). Zhu et al. (2015) show a reduction of the thickness of the ejecta blanket by 5-15% by material sliding within 1.2 transient crater radii. However, we already excluded this range from our fitting results.

In our approach, we also neglected effect of ballistic sedimentation or secondary mass wasting as described by Hörz et al. (1983). Early ejected material is fast and deposited at large radial distance. It will impact the target with an equal large velocity as during ejection, causing secondary cratering and material mixture of local target material and ejecta. Furthermore, radial momentum will cause material sliding. Both effects will change the thickness of the deposited ejecta at a given radial distance, modifying the decay behaviour of the ejecta deposit over distance. These processes depend on the velocity and mass of the ejecta that re-impacts the target and as such are size-scale depending.

Finally, our assumption of parabolic trajectories neglects effects of the interaction with an atmosphere or impact plume or possible effects of spatially varying gravity for large impact scenarios. To include such effects it is necessary to calculate trajectories within a realistic gravity field that depends on radial distance from the central body, or to model ejecta trajectories in a consistent model set-up including the interaction with the atmosphere. This interaction is size-dependent and can cause sorting of ejecta by its particle size in radial or vertical direction of the ejecta deposit, and causes deviations from the results derived by ballistic parabolas. Hence, deriving information from final ejecta blankets is a challenging task as many processes are involved in their formation, and the required measurement precision of observed ejecta blankets may prove too difficult to achieve for natural craters.

Conclusion

We performed a suite of numerical impact simulations to investigate the influence of impact velocity and target properties on ejection velocities and angles, as well as the thickness distribution of ejecta deposits. The main conclusions from our simulations are:

1. Our simulations with increasing coefficient of friction (0.0 – 1.0) show a steeper reduction in ejection velocity with launch position, consistent with the formation of smaller craters. Ejection angles also decrease, and show a decreasing spread, with

distance. This affects the ejecta deposit thickness as a function of distance: increasing the coefficient of friction leads to smaller thickness at the rim T_0 and smaller decay exponents.

2. Our simulations with increasing porosity (0% – 42%) show a reduction in proximal ejection velocities, consistent with a decrease in peak pressure owing to compaction of target porosity. Ejection angles remain similar for all porosities. The ejecta thickness is characterised by similar T_0 and decay exponent for all porosities.
3. Our simulations with increasing cohesion (0 MPa – 150 MPa) show that the craters are smaller, but ejection velocities follow the same trend with launch position until the near-rim region where ejection velocities decrease much more steeply than for the simulations with increasing coefficient of friction. The same behaviour holds true for the ejection angle that focus at ~ 45°-50°. The ejecta thickness is characterised by smaller T_0 and decay exponent.
4. Our simulations with increasing impact velocity (but approximately equal crater volumes) show that proximal ejection velocities increase. However, the ejection velocities as a function of distance follow similar trends at large launch positions. Ejection angles increase with impact velocity for our non-porous target. The ejecta thickness is characterised by similar T_0 and decay exponent for all impact velocities in the hypervelocity regime.
5. Scaling exponents μ were derived for all model data. Comparing the results for sand-like material, we see a discrepancy between the μ-value derived from ejecta distributions and from crater size. However, for sand-like material the μ-value that we derive for the ejecta distribution from numerical simulations is consistent with that measured in experiments by Cintala et al. (1999). The static point source assumption should be considered with care when applying scaling relationships for dynamic cratering phenomena, such as ejecta distributions.
6. According to our study, it appears to be possible to derive information on the target material properties based on sufficiently accurate measurements of the ejecta thickness over distance. However, sufficiently accurate measurements are difficult to achieve and modifications processes need to be considered.

Acknowledgements

This project is part of the MEMIN FOR887 and the SFB-TRR170 funded by the German Research Foundation: DFG-grants # WU 355/6-2 and A4, respectively. M. Z. is partly supported by the Science and Technology Development Fund of Macau (075/2014/A2). We thank J. L. B. Anderson and P. H. Schultz for their very constructive reviews, and Jeff Plescia for editing this article. We gratefully acknowledge the developers of iSALE-2D, including Dirk Elbeshausen, Boris Ivanov and Jay Melosh. We also acknowledge the developer of the pySALEPlot tool (who also implemented the code version of ejecta determination that we used into the iSALE source code) Tom Davison, and the developer of the VIMoD software Dirk Elbeshausen. iSALE –Website: **www.isale-code.de.**

References

Alvarellos J. L., Zahnle K. J., Dobrovolskis A. R., and Hamill P. 2008. Transfer of mass from Io to Europa and beyond due to cometary impacts. *Icarus* 194(2):636–646. doi:10.1016/j.icarus.2007.09.025.

Amsden A., Ruppel H., and Hirt C. 1980. *SALE:: A simplified ALE computer program for fluid flow at all speeds*. Los Alamos National Laboratories Report LA-8095.

Anderson J. L. B., Cintala M. J., Siebenaler S. A., and Barnouin-Jha O. S. 2007. Ejecta- and Size-Scaling Considerations from Impacts of Glass Projectiles into Sand. *Proceedings of the Lunar and Planetary Science Conference* 38:2266.

Anderson J. L. B. and Schultz P. H. 2003. Asymmetry of ejecta flow during oblique impacts using three-dimensional particle image velocimetry. *Journal of Geophysical Research* 108(E8):3987. doi:10.1029/2003JE002075.

Anderson J. L. B., Schultz P. H., and Heineck J. T. 2004. Experimental ejection angles for oblique impacts: Implications for the subsurface flow-field. *Meteoritics & Planetary Science* 39(2):303–320. doi:10.1111/j.1945-5100.2004.tb00342.x.

Anderson J. L.B. and Schultz P. H. 2006. Flow-field center migration during vertical and oblique impacts. *International Journal of Impact Engineering* 33(1-12):35–44. doi:10.1016/j.ijimpeng.2006.09.022.

Artemieva N. and Ivanov B. 2004. Launch of martian meteorites in oblique impacts. *Icarus* 171(1):84–101. doi:10.1016/j.icarus.2004.05.003.

1103 Artemieva N. A., Wünnemann K., Krien F., Reimold W. U., and Stöffler D. 2013. Ries crater
1104 and suevite revisited-Observations and modeling Part II: Modeling. *Meteoritics &*
1105 *Planetary Science* 48(4):590–627. doi:10.1111/maps.12085.
1106 Barnouin-Jha O. S. and Schultz P. H. 1996. Ejecta entrainment by impact-generated ring
1107 vortices:: Theory and experiments. *Journal of Geophysical Research* 101(E9):21,099-
1108 21,115.
1109 Buhl E., Sommer F., Poelchau M. H., Dresen G., and Kenkmann T. 2014. Ejecta from
1110 experimental impact craters: Particle size distribution and fragmentation energy. *Icarus*
1111 237:131–142. doi:10.1016/j.icarus.2014.04.039.
1112 Campo Bagatin A., Farinella P., and Petit J.-M. 1994. Fragment ejection velocities and the
1113 collisional evolution of asteroids. *Planetary and Space Science* 42(12):1099–1107.
1114 doi:10.1016/0032-0633(94)90010-8.
1115 Cintala M. J., Berthoud L., and Hörz F. 1999. Ejection-velocity distributions from impacts
1116 into coarse-grained sand. *Meteoritics & Planetary Science* 34(4):605–623.
1117 doi:10.1111/j.1945-5100.1999.tb01367.x.
1118 Collins G. S., Kenkmann T., Osinski G. R., and Wünnemann K. 2008. Mid-sized complex
1119 crater formation in mixed crystalline-sedimentary targets:: Insight from modeling and
1120 observation. *Meteoritics & Planetary Science* 43(12):1955–1977. doi:10.1111/j.1945-
1121 5100.2008.tb00655.x.
1122 Collins G. S., Melosh H. J., and Ivanov B. A. 2004. Modeling damage and deformation in
1123 impact simulations. *Meteoritics & Planetary Science* 39(2):217–231.
1124 Collins G. S., Melosh H. J., and Wünnemann K. 2011. Improvements to the ε-α porous
1125 compaction model for simulating impacts into high-porosity solar system objects.
1126 *International Journal of Impact Engineering* 38(6):434–439.
1127 doi:10.1016/j.ijimpeng.2010.10.013.
1128 Croft S. K. 1985. The scaling of complex craters. *Journal of Geophysical Research*
1129 90(S02):C828. doi:10.1029/JB090iS02p0C828.
1130 Ebert M., Hecht L., Hamann C., and Luther R. 2017. Laser-induced melting experiments:
1131 Simulation of short-term high-temperature impact processes. *Meteoritics & Planetary*
1132 *Science* 52(7):1475–1494. doi:10.1111/maps.12809.
1133 Farinella P. and Davis D. R. 1992. Collision rates and impact velocities in the main asteroid
1134 belt. *Icarus* 97(1):111–123. doi:10.1016/0019-1035(92)90060-K.
1135 Fassett C. I., Head J. W., Smith D. E., Zuber M. T., and Neumann G. A. 2011. Thickness of
1136 proximal ejecta from the Orientale Basin from Lunar Orbiter Laser Altimeter (LOLA)

data: Implications for multi-ring basin formation. *Geophysical Research Letters* 38(17):n/a-n/a. doi:10.1029/2011GL048502.

Gault D. E., Quaide W. L., and Oberbeck V. R. 1968. Impact Cratering Mechanics and Structures. In *Shock Metamorphism of Natural Materials: Proceedings of the First Conference held at NASA, Goddard Space Flight Center*, edited by French B. M. and Short N. M. Baltimore: Mono Book Corporation. pp. 87–100.

Gulde M., Kortmann L., Ebert M., Watson E., Wilk J., and Schäfer F. this issue. Robust Optical Tracking of Individual Ejecta Particles in hypervelocity Impact Experiments. *Meteoritics & Planetary Science*.

Güldemeister N. and Wünnemann K. 2017. Quantitative analysis of impact-induced seismis signals by numerical modeling. *Icarus* 296:15–27. doi:10.1016/j.icarus.2017.05.010.

Güldemeister N., Wünnemann K., and Poelchau M. H. 2015. Scaling impact crater dimensions in cohesive rock by numerical modeling and laboratory experiments. In *Large Meteorite Impacts and Planetary Evolution V: Geological Society of America Special Paper*, edited by Osinski G. R. and Kring D. A. pp. 17–29.

Hartmann W. K. 1985. Impact experiments. *Icarus* 63(1):69–98. doi:10.1016/0019-1035(85)90021-1.

Head J. N., Melosh H. J., and Ivanov B. A. 2002. Martian Meteorite Launch:: High-Speed Ejecta from Small Craters. *Science (New York, N.Y.)* 298(5599):1752–1756. doi:10.1126/science.1076469.

Hermalyn B. and Schultz P. H. 2010. Early-stage ejecta velocity distribution for vertical hypervelocity impacts into sand. *Icarus* 209(2):866–870. doi:10.1016/j.icarus.2010.05.025.

Hermalyn B. and Schultz P. H. 2011. Time-resolved studies of hypervelocity vertical impacts into porous particulate targets: Effects of projectile density on early-time coupling and crater growth. *Icarus* 216(1):269–279. doi:10.1016/j.icarus.2011.09.008.

Hermalyn B. and Schultz P. H. 2014. Effects of Target Properties on Impact Ejecta Distributions:: Time resolved Experiments and Computational Benchmarking. *Proceedings of the Lunar and Planetary Science Conference* 45:2791.

Hermalyn B., Schultz P. H., Shirley M., Ennico K., and Colaprete A. 2012. Scouring the surface: Ejecta dynamics and the LCROSS impact event. *Icarus* 218(1):654–665. doi:10.1016/j.icarus.2011.12.025.

Holsapple K. 1993. The Scaling of Impact Processes in Planetary Sciences. *Annual Review of Earth and Planetary Sciences* 21(1):333–373. doi:10.1146/annurev.earth.21.1.333.

1171 Holsapple K. A. 1981. Coupling parameters in cratering. *Earth & Space Science News -*
1172 *Transactions American Geophysical Union* 62:949.
1173 Hörz F., Ostertag R., and Rainey D. A. 1983. Bunte Breccia of the Ries:: Continuous deposits
1174 of large impact craters. *Reviews of Geophysics and Space Physics* 21(8):1667–1725.
1175 Housen K. R. 1992. Crater ejecta velocities for impacts on rocky bodies. *(Abstract)* 23th
1176 Lunar and Planetary Science Conference. Lunar and Planetary Institute, LPI,
1177 Houston:555–556.
1178 Housen K. R. and Holsapple K. A. 2011. Ejecta from impact craters. *Icarus* 211(1):856–875.
1179 doi:10.1016/j.icarus.2010.09.017.
1180 Housen K. R. and Holsapple K. A. 2012. Craters without ejecta. *Icarus* 219(1):297–306.
1181 doi:10.1016/j.icarus.2012.02.030.
1182 Housen K. R., Schmidt R. M., and Holsapple K. A. 1983. Crater ejecta scaling laws::
1183 Fundamental Forms based on Dimensional Analysis. *Journal of Geophysical Research*
1184 88:2485–2499.
1185 Hüttner R. 1969. Bunte Trümmermassen und Suevit. *Geologica Bavarica* (61):142–200.
1186 Ivanov B. A., Deniem D., and Neukum G. 1997. Implementation of dynamic strength models
1187 into 2D hydrocodes: Applications for atmospheric breakup and impact cratering.
1188 *International Journal of Impact Engineering* 20(1-5):411–430. doi:10.1016/S0734-
1189 743X(97)87511-2.
1190 Kenkmann T., Deutsch A., Thoma K., Ebert M., Poelchau M. H., Buhl E., Carl E.-R.,
1191 Danilewsky A. N., Dresen G., Dufresne A., Durr N., Ehm L., Große C., Gulde M.,
1192 Güldemeister N., Hecht L., Hiermaier S., Hoerth T., Hamann C., Kowitz A., Langenhorst
1193 F., Lexow B., Liermann H.-P., Luther R., Mansfeld U., Moser D., Raith M., Reimold W.
1194 U., Sauer M., Schäfer F., Schmitt R. T., Sommer F., Wilk J., Winkler R., and Wünnemann
1195 K. this issue. Experimental impact cratering:: A summary of the major results of the
1196 MEMIN research unit. *Meteoritics & Planetary Science*.
1197 Kowitz A., Güldemeister N., Reimold W. U., Schmitt R. T., and Wünnemann K. 2013.
1198 Diaplectic quartz glass and SiO2 melt experimentally generated at only 5 GPa shock
1199 pressure in porous sandstone: Laboratory observations and meso-scale numerical
1200 modeling. *Earth and Planetary Science Letters* 384:17–26.
1201 doi:10.1016/j.epsl.2013.09.021.
1202 Krüger T., Kenkmann T., and Hergarten S. 2017. Structural uplift and ejecta thickness of
1203 lunar mare craters: New insights into the formation of complex crater rims. *Meteoritics &*
1204 *Planetary Science* 52(10):2220–2240. doi:10.1111/maps.12925.

Luther R., Artemieva N., Ivanova M., Lorenz C., and Wünnemann K. 2017. Snow carrots after the Chelyabinsk event and model implications for highly porous solar system objects. *Meteoritics & Planetary Science*. doi:10.1111/maps.12831.

McGetchin T. R., Settle M., and Head J. W. 1973. Radial Thickness Variation in Impact Crater Ejecta:: Implications for Lunar Basin Deposits. *Earth and Planetary Science Letters* 20:226–236.

Melosh H. J. 1985. Impact Cratering Mechanics:: Relationship between the Shock Wave and Excavation Flow. *Icarus* 62:339–343.

Melosh H. J. 1989. *Impact cratering:: a geologic process*. New York: Oxford Univ. Press. 245 p.

Melosh H. J. 2007. A hydrocode equation of state for SiO_2. *Meteoritics & Planetary Science* 42(12):2079–2098.

Melosh H. J., Ryan E. V., and Asphaug E. 1992. Dynamic fragmentation in impacts: Hydrocode simulation of laboratory impacts. *Journal of Geophysical Research* 97(E9):14735. doi:10.1029/92JE01632.

Oberbeck V. R. 1975. The Role of Ballistic Erosion and Sedimentation in Lunar Stratigraphy. *Reviews of Geophysics and Space Physics* 13(2):337–362. doi:10.1029/RG013i002p00337.

Ohnaka M. 1995. A shear failure strength law of rock in the brittle-plastic transition regime. *Geophysical Research Letters* 22(1):25–28. doi:10.1029/94GL02791.

Ormö J., Melero-Asensio I., Housen K. R., Wünnemann K., Elbeshausen D., and Collins G. S. 2015. Scaling and reproducibility of craters produced at the Experimental Projectile Impact Chamber (EPIC), Centro de Astrobiología, Spain. *Meteoritics & Planetary Science* 50(12):2067–2086. doi:10.1111/maps.12560.

Piekutowski A. J. 1980. Formation of bowl-shaped craters. *(Abstract)* 11th Lunar and Planetary Science Conference. Lunar and Planetary Institute, LPI, Houston:2129–2144.

Pierazzo E., Artemieva N. A., Asphaug E., Baldwin E. C., Cazamias J., Coker R., Collins G. S., Crawford D. A., Davison T., Elbeshausen D., Holsapple K. A., Housen K. R., Korycansky D. G., and Wünnemann K. 2008. Validation of numerical codes for impact and explosion cratering:: Impacts on strengthless and metal targets. *Meteoritics & Planetary Science* 43(12):1917–1938.

Pike R. J. 1974. Ejecta from large craters on the Moon:: Comments on the Geometric Model of McGetchin et al. *Earth and Planetary Science Letters* 23:265–274.

Prieur N., Rolf T., Luther R., Werner S., and Wünnemann K. 2017. Simple craters:: Influence of target properties and crater scaling relationships. *Journal of Geophysical Research: Planets* 122:1704–1726.

Schmidt R. M. 1980. Meteor Crater:: Energy of formation - Implications of centrifuge scaling. *Proceedings of the Lunar and Planetary Science Conference* 11:2099–2128.

Schröter J. H. 1791. *Selenotopographische Fragmente zur genauern Kenntniss der Mondfläche, ihrer erlittenen Veränderungen und Atmosphäre, sammt den dazu gehörigen Specialcharten und Zeichnungen*. Lilienthal: by Joh. Georg Rosenbusch.

Schultz P. H. 1988. Cratering on Mercury:: A Relook. In *Mercury: [papers presented at the Mercury Conference, held 6 - 9 Aug. 1986 in Tucson, Ariz.]*, edited by Vilas F. Tucson, Ariz.: Univ. of Arizona Pr.

Schultz P. H. 1992. Atmospheric Effects On Ejecta Emplacement. *Journal of Geophysical Research* 97(E7):11,623-11,662.

Shuvalov V. and Dypvik H. 2013. Distribution of ejecta from small impact craters. *Meteoritics & Planetary Science* 48(6):1034–1042. doi:10.1111/maps.12127.

Sommer F., Reiser F., Dufresne A., Poelchau M. H., Hoerth T., Deutsch A., Kenkmann T., and Thoma K. 2013. Ejection behavior characteristics in experimental cratering in sandstone targets. *Meteoritics & Planetary Science* 48(1):33–49. doi:10.1111/maps.12017.

Stöffler D., Gault D. E., Wedekind J., and Polkowski G. 1975. Experimental hypervelocity impact into quartz sand:: Distribution and shock metamorphism of ejecta. *Journal of Geophysical Research* 80:4062–4077.

Thomsen J. M., Austin M. G., Ruhl S. F., Schultz P. H., and Orphal D. L. 1979. Calculational investigation of impact cratering dynamics:: Early time material motions. *Proceedings of the 10th Lunar and Planetary Science Conference* 3:2741–2756.

Tsujido S., Arakawa M., Suzuki A. I., and Yasui M. 2015. Ejecta velocity distribution of impact craters formed on quartz sand: Effect of projectile density on crater scaling law. *Icarus* 262:79–92. doi:10.1016/j.icarus.2015.08.035.

Wada K., Senshu H., and Matsui T. 2006. Numerical simulation of impact cratering on granular material. *Icarus* 180(2):528–545. doi:10.1016/j.icarus.2005.10.002.

Wegener A. 1921. *Die Entstehung der Mondkrater*. Braunschweig, Germany: Friedr. Vieweg & Sohn.

Wünnemann K., Collins G. S., and Melosh H. J. 2006. A strain-based porosity model for use in hydrocode simulations of impacts and implications for transient crater growth in porous targets. *Icarus* 180(2):514–527. doi:10.1016/j.icarus.2005.10.013.

Wünnemann K., Collins G. S., and Osinski G. R. 2008. Numerical modelling of impact melt production in porous rocks. *Earth and Planetary Science Letters* 269(3-4):530–539. doi:10.1016/j.epsl.2008.03.007.

Wünnemann K., Zhu M.-H., and Stöffler D. 2016. Impacts into Quartz Sand: Crater Formation, Shock Metamorphism, and Ejecta Distribution in Laboratory Experiments and Numerical Models. *Meteoritics & Planetary Science* (in press).

Yamamoto S., Hasegawa S., Suzuki A. I., and Matsunaga T. 2017. Impact velocity dependence of transient cratering growth. *Journal of Geophysical Research: Planets* 122(5):1077–1089. doi:10.1002/2016JE005252.

Zhu M.-H., Wünnemann K., and Artemieva N. 2017. Effects of Moon's Thermal State on the Impact Basin Ejecta Distribution. *Geophysical Research Letters* 44(22):11. doi:10.1002/2017GL075405.

Zhu M.-H., Wünnemann K., and Potter R. W. K. 2015. Numerical modeling of the ejecta distribution and formation of the Orientale basin on the Moon. *Journal of Geophysical Research: Planets* 120(12):2118–2134. doi:10.1002/2015JE004827.

Appendix

Ejection criterion

In this study we define the time of ejection as the time when ejected material reaches an altitude above the target surface of one projectile diameter. Using this criterion we allow pressure, which occasionally is present within the evolving ejecta curtain, to decrease. At this time, ejection characteristics can still be influenced by pressure gradients. We also avoid including large volumes of material from the rim area in the ejected material. At the same time the criterion is close enough to the surface that the ejecta curtain is well resolved (the curtain is resolved by fewer cells with increasing altitude) and little ejected material is neglected because it does not reach that cut-off altitude. We use a linear interpolation to derive launch positions and launch times of ejecta that correspond to the surface level. This interpolation is necessary to allow for comparison with other numerical or laboratory results. However, it can cause interpolation artefacts that affect ejection speeds and angles at the rim. Linear interpolation fails due to changing trajectory angles of material moving within the transition volume of ejecta curtain and crater rim, causing a shift of the interpolated launch distance of the ejecta relative to the real launch position.

The altitude of the ejection criterion can influence the results for ejection angles to some extent. In the section "Comparison to experimental data and scaling models" we discuss the issue of determining ejection angles. For increasing altitudes of the criterion, the resulting spread in ejection angles decreases to some extent at smaller launch positions (x/a~<4, Figure A1 i). Nevertheless, some spread does remain. The question of whether this decrease in angular spread with increasing altitude improves the accuracy of the results, or whether this behaviour is caused by numerical material transport with poorer resolution of the ejecta curtain in larger altitudes for several model iterations is difficult to answer. However, the mean angle that we derive by using a mass weighted moving average is nearly consistent for all altitudes applied (Figure A1 ii). Most of the mass is ejected with this angle. We therefore adopt the mass weighted running average to most robustly characterise the effect of material properties on ejection angles.

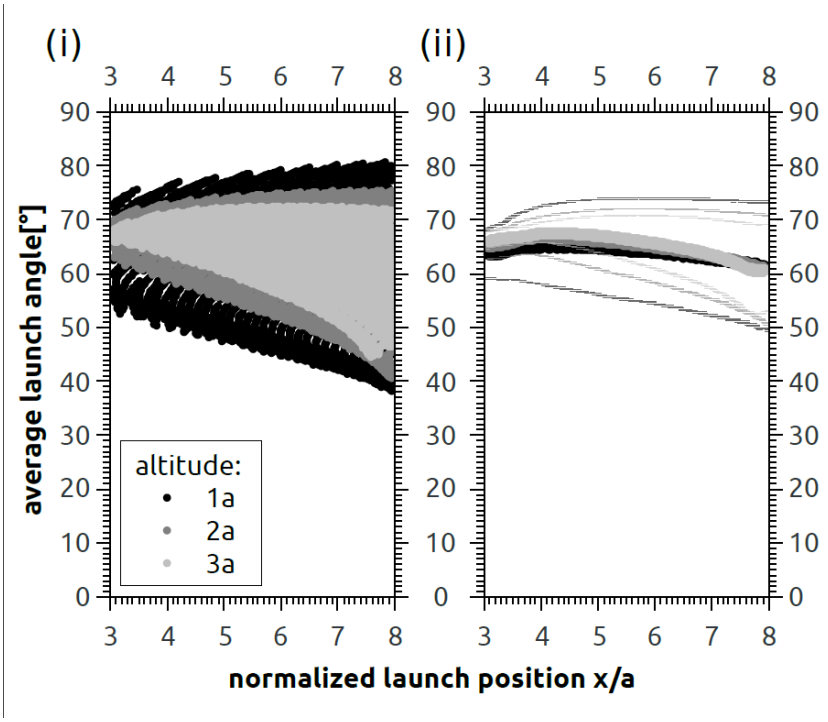

Figure A1: Launch angles (i) and mass weighted averages of launch angles (ii) for different ejection criteria. Brightening of the grey scale represents the increasing altitude of the ejection criterion. The average is shown with a mass weighted standard deviation for the data.

Resolution

We tested the sensitivity of ejection results against model resolution using 4 different resolutions between 5 and 20 CPPR for one impact scenario (Figure A2). Ejection velocities follow the same trend for all resolutions. However, the largest ejection velocities of the 5 CPPR model deviate from the velocities of the other models. Increasing the resolution from 5 to 20 CPPR shows that maximum ejection velocities seem to converge against a common value. For ejection angles, we see a similar behaviour. Ejection angles overlap for all model resolutions towards the larger launch positions. However, for the proximal range the ejection angle of the 5 CPPR model (~40°) deviates from the converging value of the 20 CPPR model (~50°). Note that increasing the model resolution includes more tracers per volume of the target material and allows for more precise assessment of material movement.

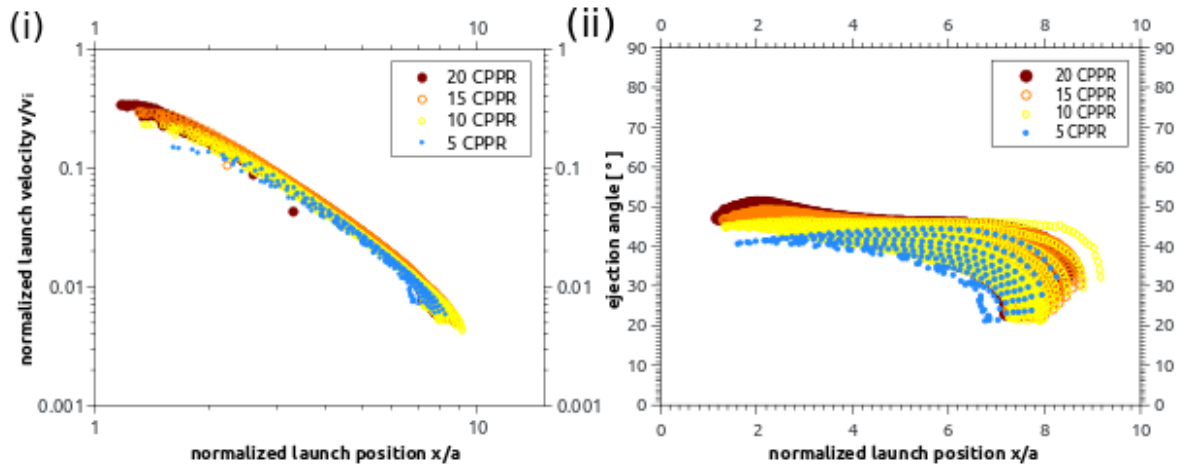

Figure A2: Launch velocity (i) and the launch angle (ii) versus launch positions on the target surface. The ejection behaviour is derived for different model resolution for equal impact scenarios. Velocity and launch position are normalised to the impact velocity and the projectile radius, respectively. Note that ejection angles are not averaged. The colour-scale corresponds to an increase in resolution from 5 CPPR to 20 CPPR.

Model Parameters

Table A1: Model parameters for all 50 models.

General parameters	
Poisson ratio (basalt)	0.3
Specific heat capacity [J/(kg K)]	800
Strength parameters	

Drucker Prager strength:	
Cohesion Y_0 [MPa]	0, 1, 10, 100, 150
Coefficient of friction μ	0.0, 0.2, 0.4, 0.6, 0.8, 1.0
Maximum strength Y_{max} [GPa]	1
Thermal Softening (Ohnaka)	
Softening constant	1.2
Melt temperate [K]**	1327
Simon approximation:	
Simon constant	$6 \cdot 10^9$
Simon exponent	3
Porosity parameters*	
Initial porosity Φ [%]	0, 10, 20, 42
Elastic volumetric threshold ε_e	-0.001
Transition distension α_x	1.1
Compaction efficiency κ	0.9
Speed of sound ratio χ	0.3

* The same porosity model parameters were used for all porosities.

**Typical range of melting temperature for rocky material (Wünnemann et al. 2008).

Unprocessed model launch angles

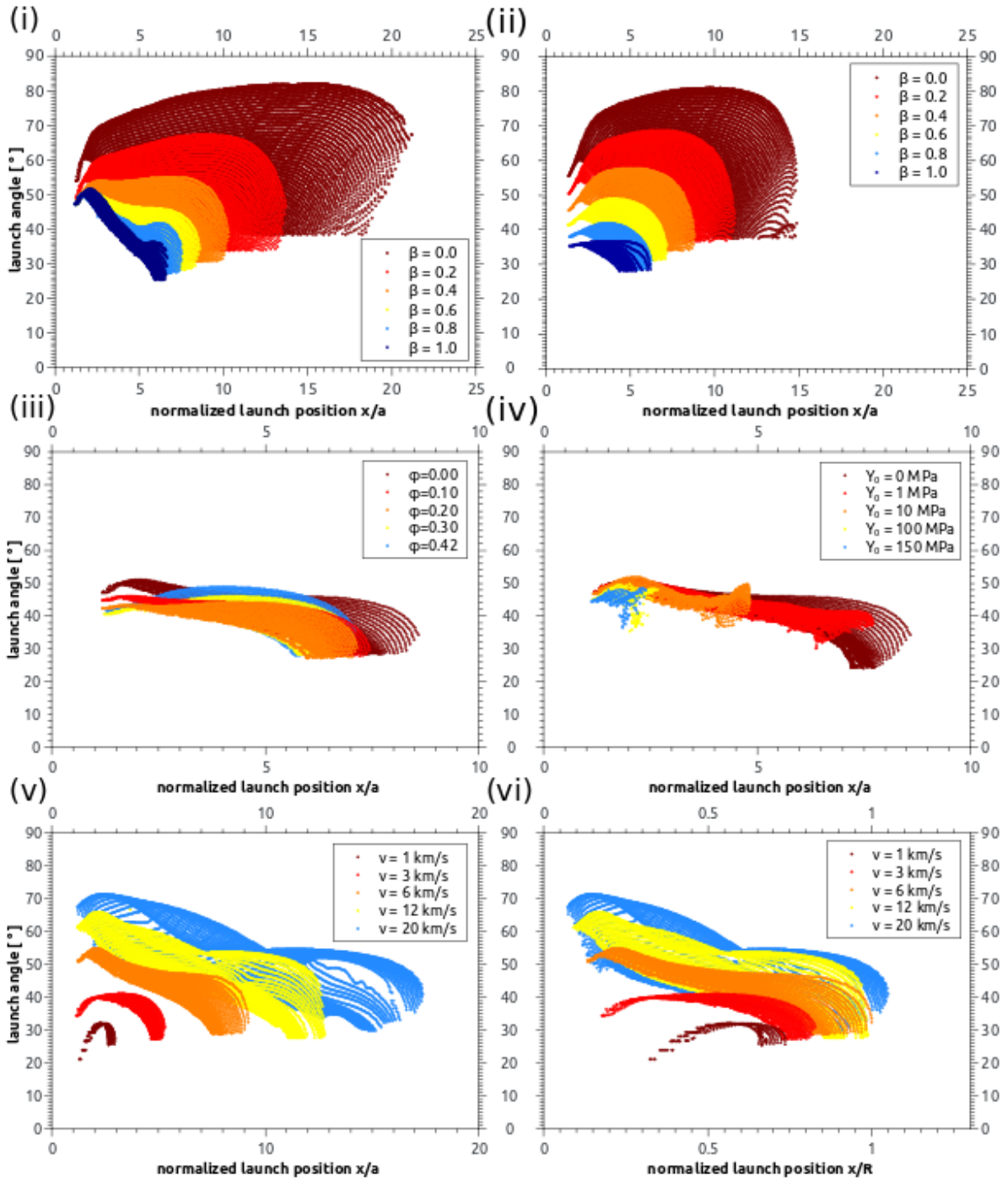

Figure S1: Unprocessed model launch angles for all scenarios from this study. (i) cohesionless, unporous target material with coefficients of friction from 0.0-1.0. (ii) cohesionless, porous (42%) target material with coefficients of friction from 0.0 – 1.0. (iii) cohesionless target material with a coefficients of friction of 0.6 and porosities from 0-42%. (iv) non-porous target material with a coefficients of friction of 0.6 and cohesions from 0-150 MPa. (v) and (vi) cohesionless, unporous target material with a coefficient of friction of 0.6 with increasing impact velocity and decreasing

projectile size, yielding equal crater volumes, shown in a normalisation for projectile size and crater radius, respectively.

Model Results - Overview

Table A2: Overview of target materials and dimensionless parameters of the models used in this study and fitting results from Eqs. (10), and (13) & (14).

Cohesion [MPa]	Coefficient of friction β	Porosity Φ	Impact velocity [km/s]	Projectile radius [m]	π_2 [10^{-5}]	π_V	Fit data: ejection velocity, Eq. (10)				ejecta deposit, Eqs. (13) & (14)		
							x-range x/R	K_3	μ		μ	B	T_0 [m]
0	0.0	0	5	25	3.159	1465.3	0.08 - 0.53	0.43	0.49	<<	0.82	3.23	22.8
0	0.2	0	5	25	3.159	458.9	0.10 - 0.56	0.53	0.49	<<	0.77	3.15	18.8
0	0.4	0	5	25	3.159	234.8	0.11 - 0.68	0.63	0.47	<<	0.67	3.01	15.1
0	0.6	0	5	25	3.159	147.4	0.13 - 0.70	0.77	0.46	<<	0.57	2.85	12.3
0	0.8	0	5	25	3.159	113.7	0.13 - 0.66	0.81	0.46	>>	0.36	2.54	6.9
0	1.0	0	5	25	3.159	99.7	0.14 - 0.64	0.82	0.47	>>	0.35	2.52	5.8
0	0.0	42%	5	25	3.159	754.9	0.10 - 0.54	0.56	0.60	<<	0.96	3.43	30.7
0	0.2	42%	5	25	3.159	335.0	0.12 - 0.55	0.59	0.60	<<	0.81	3.22	20.0
0	0.4	42%	5	25	3.159	190.6	0.13 - 0.51	0.60	0.59	<<	0.74	3.11	13.3
0	0.6	42%	5	25	3.159	128.7	0.20 - 0.53	0.70	0.62	<	0.69	3.04	9.2
0	0.8	42%	5	25	3.159	100.2	0.16 - 0.51	0.62	0.58	~	0.55	2.82	5.1
0	1.0	42%	5	25	3.159	85.8	0.16 - 0.48	0.55	0.57	>	0.51	2.76	3.1
0	0.6	10%	5	25	3.159	175.1	0.13 – 0.60	0.66	0.47	=	0.47	2.71	6.5
0	0.6	20%	5	25	3.159	157.5	0.13 - 0.56	0.62	0.49	~	0.53	2.80	6.6
0	0.6	30%	5	25	3.159	143.5	0.14 - 0.54	0.61	0.52	~	0.56	2.84	7.0
1	0.6	0	5	25	3.159	105.6	0.16 - 0.75	0.97	0.40	>>	0.22	2.33	7.4

10	0.6	0	5	25	3.159	42.8	0.23 – 0.95	2.75	0.42		- *	1.21	0.3
100	0.6	0	5	25	3.159	12.9	0.34 – 0.81	9.46	0.53		-	-	-
150	0.6	0	5	25	3.159	10.6	0.37 – 0.79	13.07	0.62		-	-	-
0	0.6	0	1	75	235.670	8.7	0.32 - 0.74	0.59	0.32	>>	0.19	2.29	4.0
0	0.6	0	3	46	16.148	50.1	0.25 - 0.70	0.76	0.43	=	0.43	2.65	11.1
0	0.6	0	6	34	2.976	166.5	0.25 - 0.73	0.85	0.48	<	0.55	2.83	19.4
0	0.6	0	12	25	0.548	474.8	0.25 - 0.69	0.86	0.52	<	0.59	2.89	22.6
0	0.6	0	20	20	0.158	949.5	0.25 - 0.70	0.86	0.52	~	0.55	2.82	20.2

* Value would be negative and is excluded. The scenario is strength dominated.